Discrete-vortical elements simulation of air jet interaction with swirling air motion inside a 2D cylinder

Asuquo B. Ebiana

Mechanical Engineering Department, Cleveland State University, Cleveland, Ohio, USA

Received April 1997
Revised October 1997
Accepted January 1998

Nomenclature

a = radius of circle in Milne-Thomson's circle theorem
C, C_1, C_2 = constants
c, s, d = Jacobian elliptic functions with real arguments (also c_1, s_1, d_1)
cn, sn, dn = Jacobian elliptic functions with complex arguments
D = finite circular domain representing the combustion chamber
D/Dt = total derivative
m = distance between mesh points
d_j = injector nozzle diameter
e_{11}, e_{12} = elements of a 2×2 matrix
$\mathbf{F}$ = matrix of geometric factors
$f(z)$ = complex potential function
G_{ij} = Green's function or vortex core smoothing function
i = grid index in the x (or ζ) direction
j = grid index in the y (or η) direction
K = the complete elliptic integral of the first kind. Also, dimension of square domain
k = modulus (a constant)
L = number of square meshes or cells within the circular domain
M = number of grid points in either ζ or η directions
$\mathbf{n}$ = unit normal vector on S
N = number of vortex elements or fluid particles
N_c = number of vortex elements required per cell
p = pressure of fluid. Also, parameter of interest
R = radius of combustion chamber
Re = Reynolds number
r_0 = discrete-vortical element's core radius
r^* = dimensionless coordinate r/R.
$\mathbf{S}$ = matrix of discrete-vortical element strengths
S = boundary of circular domain
S' = boundary of square domain
S_θ = swirl strength (cm.m/s)
t = time
Δt = length of time step
t^* = artificial time characterizing complete diffusion
U_{in} = inlet jet velocity
u = velocity component in the x-direction
v = velocity component in the y-direction
$\mathbf{V}=(u,v)$ = velocity vector
V_r = radial velocity component
V_θ = tangential velocity component
$\overline{V}_\theta$ = average tangential velocity
$\mathbf{V}_\theta$ = matrix of tangential velocity components
$W(z)$ = complex potential function
$\mathbf{x}=(x,y)$ = position vector
(x,y) = Cartesian coordinates in the circular domain
$z=x+iy$ = space coordinate in the complex circular plane

Greek symbols

α = dummy variable
β = average distance between vortices
Δt = length of time step
δ_n = numerical boundary layer thickness
∇ = the del operator
∇^2 = the Laplacian operator
ε = initial distribution of vorticity

International Journal of Numerical Methods for Heat & Fluid Flow
Vol. 8 No. 6, 1998, pp. 599–650.

Γ = the coefficient of molecular diffusion
γ_j = circulation of vortex j
O = of the order of
$\kappa = \gamma_j/2\pi$ = strength of vortex j
ν = kinematic viscosity of fluid
θ_j = angle of injection
$\omega = \zeta + i\eta$ = space coordinate in the complex square plane
$\Phi(\phi_1,\phi_2,\ldots,\phi_\sigma)$ = set of σ-dimensional scalars
ϕ = velocity potential. Also, scalar function
φ = filter function
ρ = density of fluid
σ = number of independent scalar species. Also, standard deviation (variance = σ^2)
ψ = stream function
ξ = z-component vorticity
(ζ,η) = non-dimensional Cartesian coordinates in the square domain

Subscripts

0 = initial parameter
1 = for constants and functions
α = variable parameter, $\alpha = 1,2,\ldots,\sigma$
A = valve lip region
B = valve seat region
i = index in the x(or ζ) direction
j = index in the y(or η) direction. Also, jet
m = minus
p = plus. Also, parameter of interest and discrete-vortical element
r = radial component
s = source
θ = tangential
ξ = vorticity.

Superscripts

σ = number of scalar species
$\bar{}$ = mean
$'$ = fluctuating component. Also, transformed boundary

Abbreviations

FFT = fast Fourier transform
2D = two dimensions
VAX/VMS = virtual architecture extended/ virtual memory system

Introduction

The objective of this investigation is to numerically simulate the bulk diffusion of an inert scalar field resulting from the interaction of a jet flow and a swirling cross flow inside a two-dimensional cylinder. This will be done using the merging and interaction mechanisms of discrete vortices (vorticity functions with finite cores). Studies on the dynamics of vortices are used as an idealization for improved design of certain vortex-related devices and for understanding the physics of turbulent flows. For example, a detailed understanding of the fuel/oxidizer distribution produced by the interaction of the fuel injection process and the complex aerodynamic flow associated with a combustor, allows optimal combustor design concepts to be explored in search of higher efficiency, lower emissions and greater fuel flexibility. Also the modeling of the dispersion of air and water-borne contaminants via the dynamics of vortex-body interaction has become a routine method for air and water quality management.

Calculations using vortices to simulate fluid motion have a long history of evolution from Rosenhead's (1931) hand calculations using a few line vortices to recent computer calculations involving hundreds of thousands of vortices (Koumoutsakos and Sheils, 1996; Meneghini and Bearman, 1995; Winckelmans and Leonard, 1993). Most of the earlier efforts (Abernathy and Kronauer, 1962; Rosenhead, 1931; Takami, 1964) were directed toward understanding the time evolution of finite-area vorticity regions or initial break up of the shear layer in an inviscid, incompressible fluid. Poor convergence results due to difficulties with the velocity divergence near the line vortex center rendered the classical line vortex method unreliable.

Chorin and Bernard (1973) initiated a resurgence of interest in the use of vortex methods, for modeling high Reynolds number flows of practical significance, when they suggested the use of discrete vortices for smoothing the singularity associated with line vortices. In Chorin's scheme, the vorticity in the fluid and in the boundary layer is subdivided into discrete vortices, and the equations of motion are solved by following the vortices throughout the fluid. Chorin (1973) improved the convergence of flow past a circular cylinder by an appropriate choice of the core or "cutoff" radius. Chorin (1978) further improved the slow rate of convergence near solid boundaries when he introduced a vortex sheet algorithm to generate finite vortex sheets only as needed to satisfy the no-slip boundary conditions in the surrounding potential flow.

Modern advances in computers and computational techniques on the one hand and experimental measurements and data processing on the other hand have led to a revolution both in the understanding of large scale coherent vortex structures (eddies) in turbulent flows and in predictive methods for application in technology. Several researchers (Park *et al.*, 1994; Schadow, 1989; Sung, 1994) have proposed flow simulation, mixing and combustion models based on the creation, evolution, interaction and decay of these eddies.

A comprehensive review of the general class of vortex methods which should serve as a good entry point into the literature is given by Leonard (1980). Anderson and Greengard (1985) provide another notable review. A literature search shows that the majority of the calculations using discrete vortices have been performed for external flows. The method has not been extensively applied to problems involving internal flows.

Problem formulation

A sketch of the flow geometry is shown in Figure 1. The two-dimensional cylinder is represented by the finite circular domain D with boundary S. The parameter δ_n is the numerical boundary layer thickness. The air jet is introduced at an adjustable angle ($0° < \theta_j < 180°$) into the cylinder through a nozzle orifice located on the cylinder wall. The injector nozzle valve is modeled as a single port with diameter d_j. The valve face, whose lip and seat are identified as A and B respectively, is capable of closing the inlet flow area.

At any point in the non-reactive flow system, the state of the fluid can be characterized by the velocity $\mathbf{V}$, the pressure p and a set of scalars $\Phi = (\phi_1, \phi_2, \ldots, \phi_\sigma)$ representing the species mass fractions; σ is the number of independent species. Consequently, the theoretical formulation will consider a system of equations composed of the conservation of mass, momentum and scalar species. The effort to solve a set of transient 3D simultaneous partial differential equations is beyond the scope of the present work. Therefore, a simplified, yet realistic, 2D model becomes necessary. To allow the simplification of the governing equations, the controlling features of the problem are restricted to constant pressure, single phase, incompressible mean flow formulation. Since the primary focus of this investigation is on bulk diffusion effects resulting from the interaction of the swirl and jet vortices, turbulent and molecular diffusion

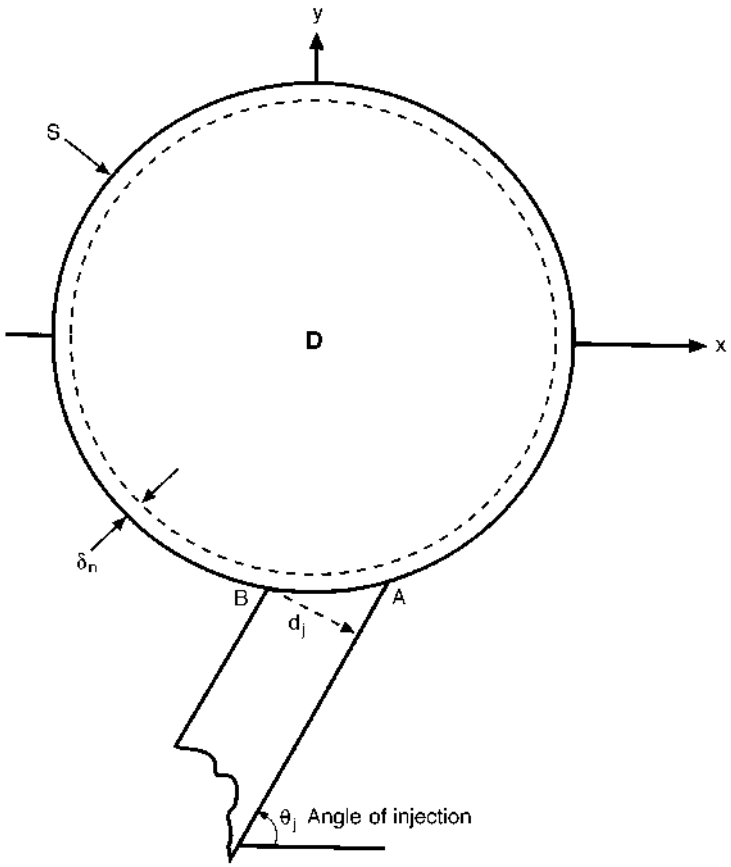

Figure 1.
Sketch of flow geometry

effects will be neglected. A future study will attempt to incorporate these effects. Also, due to difficulties with wall convergence, calculations will be limited to the interior flow domain away from the boundary layer region.

The two-dimensional calculations presented herein employ the discrete-vortical element method developed by Chorin in conjunction with the Vortex-In-Cell (VIC) solution technique to approximate the mean flow generated by the primary air swirl inside the cylinder. A discrete jet model analogous to Ashurst's (1981) scheme is used to approximate the jet flow.

Air swirl

As a consequence of the idealizations discussed above, the conservation of mass and the Navier-Stokes equations governing the flow field can be expressed in the following simple forms:

$$\nabla \cdot \boldsymbol{V} = 0 \tag{1}$$

$$\frac{D\mathbf{V}}{Dt} = -\frac{\nabla p}{\rho} + \nu\nabla^2\mathbf{V} \tag{2}$$

where $\mathbf{V}=(u, v)$ is the velocity vector, ν, ρ and p are the kinematic viscosity, density and pressure of the fluid, respectively. $D/Dt = \partial/\partial t + \nabla\cdot\mathbf{V}$ is the total derivative, ∇ is the del operator and ∇^2 is the Laplacian operator. The flow field is satisfied by the solution of these equations in the finite circular domain D with appropriate boundary conditions.

The curl of equation (2) eliminates the pressure and gives the vorticity transport equation

$$\frac{D\xi}{Dt} = \nu\nabla^2\xi \tag{3}$$

where the vorticity

$$\xi = \partial_x v - \partial_y u \tag{4}$$

The initial condition $\xi(x, y, t = 0)$ is assumed known in D. The coordinates x and y are cartesian coordinates and t is time. The discrete-vortical element formulation makes use of the simplified system of equations which now consists of equations (1), (3) and (4) to describe the flow.

A convenient solution device is the operator splitting technique, discussed extensively by Yanenko (1971), whereby the transport of vorticity (equation 3) can be implemented in two fractional steps: advection and diffusion. The component equations are respectively

$$\frac{D\xi}{Dt} = 0 \tag{5}$$

$$\partial_t\xi = \nu\nabla^2\xi \tag{6}$$

This technique permits the application of the most efficient numerical algorithm to compute each part independently and in succession. The combination of the solutions of the advection and diffusion equations produces an approximation to the solution for the full flow.

The Euler equation (equation 5) is equivalent to the statement that the conserved vorticity field is advected by its own velocity field. The divergence free velocity field can be constructed from the vorticity distribution by superposing the velocity field produced by each individual vortex. An initial distribution of discrete vortices is selected so that an approximation to the vorticity field is obtained. Since the flow under study is incompressible and two-dimensional, the velocity components u and v can be expressed in terms of the streamfunction ψ as follows:

$$u = \partial_y\psi \quad ; \quad v = -\partial_x\psi \tag{7}$$

and from equation (4)

$$\nabla^2 \psi = -\xi \tag{8}$$

with the normal boundary condition **V** • **n** = 0 where **n** is the unit normal vector on S. Equation (8) is used to determine ψ up to an additive constant. In terms of the classical Green's function, it is given by

$$\psi = \sum_{\substack{j=1 \\ j \neq i}}^{N} G_{ij}(z_i - z_j)\kappa_j \tag{9}$$

where N is the number of vortices, $z_i = (x_i, y_i)$ is the ith point of interest in the flow domain, $z_j = (x_j, y_j)$ is the position of the jth vortex, $G_{ij}(z_i - z_j)$ is the Green's function and $\kappa_j = \gamma_j/2\pi$ is the strength of vortex j. The parameter γ_j is the circulation of vortex j. If the normal boundary condition is to hold, then at the boundary, the streamfunction must satisfy ψ = constant.

Each vortex is moved by the velocity field induced by all the other vortices. Thus combining equation (7) with equation (9) we get

$$u_j = \sum_{\substack{j=1 \\ j \neq i}}^{N} \partial_y G_{ij}(z_i - z_j)\kappa_j \tag{10}$$

$$v_j = -\sum_{\substack{j=1 \\ j \neq i}}^{N} \partial_x G_{ij}(z_i - z_j)\kappa_j \tag{11}$$

where u_j and v_j are the velocity components at the vortex position in the cartesian coordinate system. To advance the vorticity to the next time step, the velocity is calculated at the current position of each discrete-vortical element and using an appropriate time integration scheme, the convection step is accomplished.

It has long been known that the convergence of the flow fields (u_j, v_j) to the exact solutions is rather poor; the reason is connected with the singularity in the velocity field at the vortex positions, i.e. when $z_i = z_j$. An obvious modification of the method is to pick $|z_i - z_j|$ small but not zero, and ensure that **V** remains smooth as $z_i \rightarrow z_j$. The techniques for doing this are implicit in the work of Hald and Del Prete (1978), Millinazzo and Saffman (1978) or Beale and Majda (1982). The form of the vortex core smoothing function or Green's function $G_{ij}(z_i - z_j)$ given by Hald and Del Prete and employed in this study is

$$G_{ij} = \begin{cases} \left[C_1\left(1 - \dfrac{|z_i - z_j|^3}{r_0^3}\right) - C_2\left(1 - \dfrac{|z_i - z_j|^2}{r_0^2}\right) + \log r_0\right]; & |z_i - z_j| \leq r_0 \\ (z_i - z_j)^{-1} & ; \quad |z_i - z_j| > r_0 \end{cases} \tag{12}$$

where r_0 is the core or "cut-off" radius of the vortex, $C_1 = 2/3$ and $C_2 = 3/2$.

The appearance of the vorticity diffusion term in equation (6) has two ramifications: vorticity creation at the boundary and diffusion of concentrations of vorticity in the flow field. Chorin (1973; 1978) has constructed a vorticity creation algorithm at the boundary using vortex sheets and suggested that viscous diffusion in both the interior and boundary layer regions can be incorporated as a dispersion of vorticity by random walk simulation at each time step, Δt. Assuming discrete vortical elements are already present in the computational domain, their positions after advecting and diffusing for a time Δt are given by

$$\begin{aligned} x_j^{n+1} &= x_j^n + u_j^n \cdot \Delta t + \eta_1 \\ y_j^{n+1} &= y_j^n + v_j^n \cdot \Delta t + \eta_2 \end{aligned} \tag{13}$$

The random variables η_1, η_2 are to be drawn from a Gaussian distribution with zero mean and a variance that grows with time as $2\nu\Delta t$. The idea is that the effects of real viscosity are correctly reproduced in a statistical sense. Chorin's (1973) random walk scheme is employed in this study to model viscous diffusion of vorticity in the interior flow domain.

The application of Green's function formulation is clearly troubled by source singularities and by long running times since a large number of vortices is required for reasonable accuracy and $O(N^2)$ interactions must be computed per time step. This study circumvents these problems by employing the Vortex-In-Cell (VIC) formulation for the numerical approximation of the velocity field.

The VIC technique essentially combines the best features of the vortex tracking concept of the discrete vortices with the steamfunction-vorticity finite-difference method. The inversion of Poisson's equation (equation 8) is performed on a uniform square grid superimposed over the vortices by using a Fast Fourier Transform (FFT) method whose work load increases linearly with the number of vortex elements. At the beginning of each time step, a numerical filter or shape function is applied to each vortex element to temporarily create a mesh record of the vorticity field. This eliminates the singularity associated with the vortex position. Next, a centered difference technique, which assures local conservation of mass, is applied to the mesh record of the streamfunction resulting from Poisson inversion to obtain local effects of the velocity field. The filter, again, provides the means for interpolating the local effects of the velocity field from the grid to the vortex positions which are now updated. The procedure is repeated each time step until the flow evolution is completed.

It turns out that interpolation to and from the grid are the most sensitive procedures of the VIC algorithm. The choice of a good numerical filter (Ebiana and Bartholomew, 1996) is therefore crucial in the successful implementation of the VIC algorithm. This study employs Couet's filter (Couet *et al.*, 1981):

$$\varphi(\eta) = \begin{cases} \frac{1}{2}\left(\frac{3}{2} - |\eta|\right)^2 & ; \frac{1}{2} \le |\eta| \le \frac{3}{2} \\ \frac{3}{4} - \eta^2 & ; |\eta| \le \frac{1}{2} \\ 0 & ; \textit{otherwise} \end{cases} \tag{14}$$

to distribute the vorticity from each vortex over the nearest three grid points in a given coordinate direction. The parameter η is a dimensionless coordinate.

Air jet

The scalar field $\phi_\alpha(\mathbf{x}, t)$ ($\alpha = 1, 2, \ldots, \sigma$) in an incompressible flow subject to a velocity $\mathbf{V}(\mathbf{x}, t)$ and undergoing Fickian molecular diffusion is governed by the scalar conservation equation:

$$\rho\left[\frac{\partial \phi_\alpha}{\partial t} + V_i \frac{\partial \phi_\alpha}{\partial x_i}\right] = \frac{\partial}{\partial x_i}\left(\Gamma \frac{\partial \phi_\alpha}{\partial x_i}\right) \tag{15}$$

where $\rho(\Phi)$ is the density, $\Phi_\alpha = (\phi_1, \phi_2, \ldots, \phi_\alpha)$ is the set of σ-dimensional scalars representing the species mass fractions, $\mathbf{V}_i(\mathbf{x}, t)$ is the ith component of the prescribed velocity vector field and Γ is the coefficient of molecular diffusion. Summation convention over repeated indices is implied.

Since, for simplicity, an air jet is assumed, the scalar transport equation (15) reduces to an equation analogous to equation (3):

$$\frac{D\phi_\alpha}{Dt} = \nu \nabla^2 \phi_\alpha \tag{16}$$

The initial scalar composition $\Phi_\alpha(\mathbf{x}, 0)$, ($\alpha = 1, 2$) are established by an air particle injection process. The dynamics of the injected air particles are analyzed using a discrete jet model analogous to Ashurst's (1981) scheme.

At each time step, the jet flow is simulated using two discrete vortices, one created at the valve lip (region A) and the other created at the valve seat (region B) (see Figure 1) with the appropriate sign and strength for the circulation given as (Ashurst, 1981):

$$\kappa_A = -\frac{U_{in}^2}{2}\Delta t \quad ; \quad \kappa_B = +\frac{U_{in}^2}{2}\Delta t \tag{17}$$

where U_{in} is the inlet jet velocity, κ_A is the source strength at the valve lip and κ_B is the source strength at the valve seat. Since the boundary layer region is not considered in this analysis, the particles are injected with initial velocity sufficient to clear the numerical boundary layer thickness $\delta_n = 3\sqrt{2\nu\Delta t}$. At the end of the intake flow simulation, the valve face is closed and represented as a solid wall. Note that for the duration of the injection process, the number of

vortices in the system increases by two at each time step and the velocity field has two parts:

$$V(x,y) = V_\xi + V_s \tag{18}$$

where $\mathbf{V}_\xi$ is the velocity produced by all the vorticity that is already in the system and $\mathbf{V}_S$ is the velocity produced by the source represented by the two discrete vortices at the inlet flow area. The distribution of the jet vortices in the system at later times is obtained by letting the vortices move with the swirling fluid.

Exact solution

The basis for the simulation is discussed and tested against theoretical results for the velocity field and streamfunction obtained by the method of images. A modified circle theorem of Milne-Thomson (1940) is employed for the velocity field in the circular domain. The circle theorem states in essence that a flow field's complex potential $f(z)$ will, upon the introduction of a circular cylinder into the field of flow, be modified to

$$W(z) = f(z) + \overline{f}\left(\frac{a^2}{z}\right) \tag{19}$$

where the overbar signifies the complex conjugate of the complex function f and a is the radius of the circular cross-section of the cylinder. Since all singularities of $f(z)$ are by hypothesis exterior to the circle, all the singularities of $\bar{f}(a^2/z)$ are interior to the circle.

Consider the application of the theorem to the flow modeled by a single point vortex j with complex potential given by

$$f(z) = -i\kappa_j \ln(z - z_j) \tag{20}$$

By the circle theorem, the complex potential of the flow becomes

$$W(z) = -i\kappa_j \ln(z - z_j) + i\kappa_j \ln\left(\frac{a^2}{z} - \overline{z_j}\right) \tag{21}$$

which can be rearranged to give

$$W(z) = -i\kappa_j\left[\ln(z - z_j) - \ln\left(\frac{a^2}{\overline{z_j}} - z\right) + \ln\left(\frac{z_j}{z}\right)\right] \tag{22}$$

On the right hand side of equation (22), the first term represents the contribution of the vortex outside of the circle, the second term is the image vortex located inside the circle, and the final term, which can be neglected for internal flows, is a vortex located at the origin to preserve the net circulation in the computational domain. With this modification, the complex potential becomes

$$W(z) = -i\kappa_j\left[\ln(z-z_j) - \ln\left(\frac{a^2}{\overline{z_j}}-z\right)\right] \tag{23}$$

The velocity field produced by this complex potential can be expressed as

$$[u - iv]_j = \frac{dW(z)}{dz} = -i\kappa_j\left[\frac{1}{(z - z_j)} - \frac{1}{(z - \frac{a^2}{\overline{z_j}})}\right] \tag{24}$$

The singularities are smoothed using equation (12). The velocity field due to a collection of vortices can be constructed through superposition:

$$[u - iv]_k = \sum_{\substack{j=1 \\ j\neq k}}^{N} -i\kappa_j\left[\frac{1}{(z_k - z_j)} - \frac{1}{(z_k - \frac{a^2}{\overline{z_j}})}\right] \tag{25}$$

where the velocity at any point z_k inside the circular domain is the sum of the velocities due to all vortices located at z_j.

A similar construction for the streamfunction in the square domain gives (see Appendix):

$$\psi = \frac{\kappa}{2}\ln\left[\frac{\sinh^2(\zeta_m) + \sin^2(\eta_p)}{\sinh^2(\zeta_m) + \sin^2(\eta_m)}\right] \tag{26}$$

where

$$\zeta_m = \frac{\pi}{2K}(\zeta-\zeta_0), \quad \eta_m = \frac{\pi}{2K}(\eta-\eta_0) \quad \textit{and} \quad \eta_p = \frac{\pi}{2K}(\eta+\eta_0)$$

The parameters ζ and η are non-dimensional coordinates with ζ_0, η_0 specifying the location of the real vortex in the square domain. The subscripts *m* and *p* correspond, respectively, with the minus and plus signs associated with the arguments.

Numerical considerations

Point vortex initialization scheme

The vorticity field at the initial time can be approximated using discrete vortices in two ways. The first scheme involves analyzing the problem from the point in time when the mechanism that is responsible for the production of vorticity within the boundary layer first introduced vorticity into the interior domain to the point where the flow field matches the desired initial conditions. This method is computationally expensive. It would be computationally more advantageous to develop a method that generates the initial distribution and strengths of the vortices directly from a prescribed velocity field, or alternately, from the derivative of the prescribed velocity field. In either case an iterative method is implied.

The initialization scheme employed in this study makes use of the tangential velocity field prescribed by the experimental data of Dyer (1978). The optimum distribution and strengths of the discrete vortices are determined from the prescribed velocity data as follows:

(1) Discrete-vortical elements are arbitrarily but uniformly placed in concentric circles about the origin of the circular domain.

(2) A modified circle theorem of Milne-Thomson is applied to the system of vortices to compute the strengths of the vortices.

(3) The optimum distribution is found when the sum of the circulation due to each vortex is equal to the global circulation $2\pi R\bar{V}_\theta$, i.e.

$$\sum_{j=1}^{N} \gamma_j = 2\pi R\bar{V}_\theta \quad or \quad \sum_{j=1}^{N} \kappa_j = R\bar{V}_\theta \tag{27}$$

where N is the number of vortices, γ_j is the circulation of vortex j, κ_j is the strength of vortex j, R is the chamber radius and V_θ is the average tangential velocity obtained by numerically integrating the prescribed velocity data.

To obtain the strengths of the vortices, consider an arbitrary distribution of the vortices as noted above. From equation (25), the velocity at any point z_k inside the circular domain is:

$$[u - iv]_k = \sum_{\substack{j=1 \\ j \neq k}}^{N} - i\kappa_j \left[\frac{1}{(z_k - z_j)} - \frac{1}{(z_k - \frac{R^2}{\bar{z}_j})} \right] \tag{28}$$

Equation (28) is composed of three factors: the desired velocity $(u - iv)_k$, the discrete-vortical element strength κ_j and a geometric factor relating the influence of vortex j at point z_k. This information can be represented in matrix form as

$$(V_\theta)_k = F_{kj} S_j \tag{29}$$

where $(\mathbf{V}_\theta)_k$, $\mathbf{F}_{kj}$, $\mathbf{S}_j$ are matrices for the prescribed tangential velocities of the swirl at the points z_k, geometric factors and vortex strengths respectively. Solving for the strengths by inverting the $\mathbf{F}_{kj}$ matrix, we get:

$$S_j = F_{kj}^{-1} (V_\theta)_k \tag{30}$$

Different initial swirl conditions are represented by Dyer's data in Table I. The data is classified according to a time τ_0 which is the time from the closing of the shrouded intake valve to the time of measurement.

The computational analyses were conducted on the VAX/VMS system. The results from the vorticity initialization program are presented in Tables II(a)

r/R	$\overline{V_\theta}$ (m/s) τ_0 (m/s) 100	150	200	300	500
0.125	12.00	8.60	7.30	5.30	3.50
0.200	24.50	14.70	12.60	10.00	4.90
0.300	33.10	21.60	16.60	11.40	5.50
0.400	37.20	25.10	17.00	10.30	5.20
0.500	39.00	23.90	16.30	9.60	4.90
0.600	37.60	22.20	15.10	9.00	4.70
0.700	33.70	20.40	14.00	8.40	4.50
0.800	30.00	18.80	13.10	7.80	4.30
0.900	28.20	17.35	12.40	7.60	4.30
0.950	27.80	17.00	12.10	7.50	4.30
Average (m/s)	27.80	17.50	12.50	7.90	4.10

Notes:
$\overline{V_\theta}$ = Mean tangential velocity (m/s)
r = Radial distance (cm)
R = Chamber radius (cm)
τ_0 = Time from the closing of the shrouded intake valve to time of measurement

Table I.
Dyer's experimental data

and II(b). Table II(a) illustrates the vorticity field iteration data for τ_0 = 100ms. Note that the vorticity field initialization was achieved at the 13th iteration. This procedure is representative of similar iterations performed for $100 \leq \tau_0 \leq$ 500ms. The initialization results for the different times are presented in Table II(b). The parameters μ and σ are the mean value and standard deviation of the strengths of the vortices respectively.

Figure 2 illustrates the optimum geometric distribution of the system of 105 discrete vortices for τ_0 = 100ms. This initialization scheme successfully reproduced Dyer's velocity profiles which are illustrated in Figure 3. It should be mentioned that the iteration procedure is open ended such that the number of vortices and geometric distribution for each τ_0 are not unique. The iterations were performed with a view toward minimizing the number of vortices since the computational work load is $O(N^2)$ for the exact solution scheme.

Conformal transformation

Conformal transformation provides the flexibility for performing calculations in a simpler domain. In this study, conformal transformation of position and velocity is a necessary requirement imposed by the choice of the VIC formulation. The VIC algorithm is implemented on a uniform square grid, mesh size $m \times m$, and the resulting velocity field is transformed onto an equivalent non-uniform grid system in the circular domain in order to advance the solution in time. Computational economy dictates that only the mesh record of the grid point position and velocity information be transformed. Information at off-grid locations is obtained via an interpolation scheme.

									$(\sum \kappa_j)$ desired =		$R\overline{V_\theta}$ = 27.80cm. m/s		$\mu = \frac{\sum \kappa_j}{N}$						
									R = 1.0 cm		$\overline{V_\theta}$ = 27.80 m/s		$\sigma^2 = \langle \frac{\sum \lvert\kappa_j\rvert^2}{N} \rangle - \mu^2$						
					r/R														
					Point vortex distribution														
Trial No.	0.1	0.2	0.3	0.4	0.5	0.6	0.7	0.8	N	$\sum \kappa_j$	$\lvert\kappa_j\rvert_{min}$	$\lvert\kappa_j\rvert_{max}$	μ	$\frac{\sigma}{\mu}$					
1	6	10	10	12	24	32	24	10	128	26.07	0.09	0.72	0.20	0.71					
2	6	10	10	12	24	32	26	10	130	26.18	0.10	0.72	0.20	0.72					
3	6	10	10	12	24	32	22	10	126	25.96	0.09	0.73	0.21	0.71					
4	6	10	10	12	24	32	32	10	136	26.50	0.10	0.72	0.19	0.74					
5	4	6	6	7	28	32	28	8	119	28.72	0.11	1.03	0.24	0.77					
6	4	6	6	7	28	32	30	8	121	28.86	0.11	1.03	0.24	0.77					
7	4	6	6	7	28	32	26	8	117	28.59	0.11	1.03	0.24	0.76					
8	4	6	6	7	28	32	20	8	111	28.17	0.11	1.04	0.25	0.75					
9	4	6	6	7	28	32	14	8	105	27.75	0.10	1.05	0.26	0.73					
10	4	6	6	7	28	32	12	8	103	27.60	0.10	1.05	0.27	0.72					
11	4	6	6	7	28	32	16	8	107	27.89	0.10	1.05	0.26	0.73					
12	4	6	6	7	28	32	15	8	106	27.82	0.10	1.05	0.26	0.73					
13	4	6	6	6	28	32	15	8	105	27.80	0.10	1.06	0.26	0.73					

Table II(a).
Velocity field initialization iteration data (τ_o = 100ms)

Time (ms)	r/R Point vortex distribution 0.1	0.2	0.3	0.4	0.5	0.6	0.7	0.8	N	$(\sum \kappa_j)$ desired $\sum \kappa_j$	$\lvert\kappa_j\rvert_{min}$	$\lvert\kappa_j\rvert_{max}$	μ	$\frac{\sigma}{\mu}$
100	4	6	6	6	28	32	15	8	105	27.80	0.10	1.06	0.26	0.73
150	4	6	6	8	31	32	15	8	110	17.50	0.02	0.55	0.16	0.73
200	4	6	6	13	31	32	15	8	115	12.50	0.05	0.43	0.11	0.74
300	4	6	6	16	34	34	18	8	126	7.90	0.03	0.34	0.06	0.84
500	4	6	6	6	26	30	16	8	102	4.10	0.03	0.22	0.04	0.86

$(\sum \kappa_j)$ desired:
@ 100ms = 27.80cm. m/s
@ 150ms = 17.50cm. m/s
@ 200ms = 12.50cm. m/s
@ 300ms = 7.90cm. m/s
@ 500ms = 4.10cm. m/s

Table II(b).
Velocity field initialization data ($100\text{ms} < \tau_0 < 500\text{ms}$)

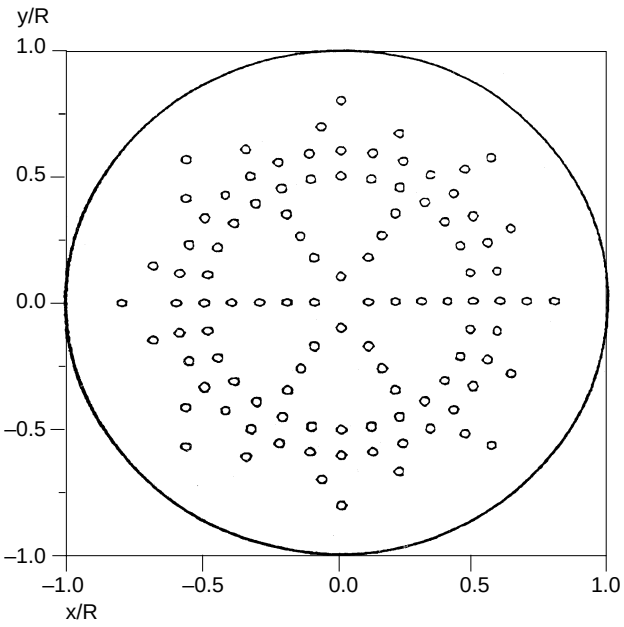

Figure 2. Geometric distribution of the system of 105 discrete vortices (τ_0 = 100ms)

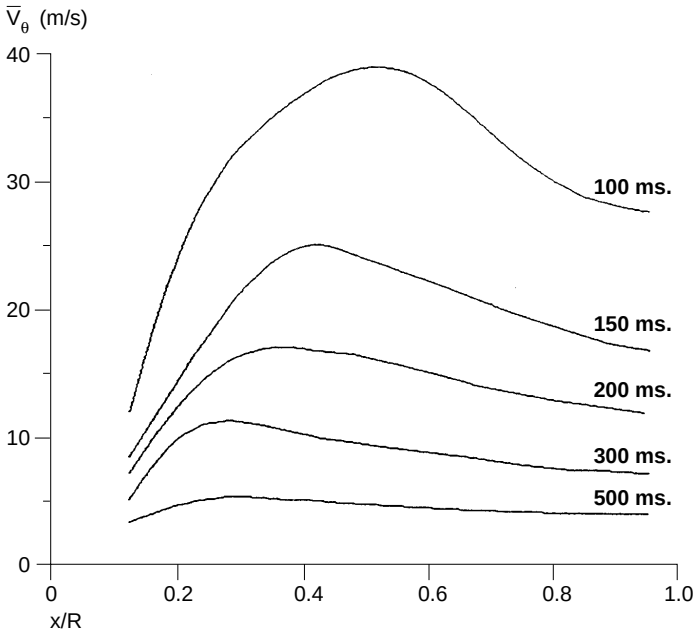

Figure 3. Radial distribution of tangential velocity component

Grid transformation

The basis for the transformability of the grid systems shown in Figure 4 is provided by the equation (Bowman, 1961):

$$z = \frac{sn(\omega)\, dn(\omega)}{cn(\omega)} \tag{31}$$

where $z = x + iy$ and $\omega = \zeta + i\eta$; the coordinates (x, y) and (ζ, η) are non-dimensional grid point coordinates in the circular and square domains with boundaries S and S' respectively; the functions $cn(\omega)$, $dn(\omega)$ and $sn(\omega)$ are Jacobian elliptic functions with complex arguments.

The transformation (31) will transform the square $-K/2 \leq \zeta\ K/2$, $-K/2 \leq \eta\ K/2$ onto the unit circle $|z| = 1$. The length of the square K is the value of the complete elliptic integral of the first kind defined as

$$K = \int_0^{\frac{\pi}{2}} \frac{d\alpha}{\sqrt{1 - k^2 \sin^2 \alpha}} \tag{32}$$

where the modulus k is a constant and α is a dummy variable. K is evaluated using Gauss-Legendre quadrature. The square domain is divided into $M \times M$ grid squares giving the grid point coordinates (ζ, η). M is the desired number of grid points in the ζ and η directions. The corresponding grid point coordinates (x, y) in the circular domain are determined by first reducing equation (31) into a system of non-linear algebraic equations of the form

$$x = f(c, c_1, d, d_1, s, s_1, k) = f(\zeta, \eta, k) \tag{33}$$

$$y = g(c, c_1, d, d_1, s, s_1, k) = g(\zeta, \eta, k) \tag{34}$$

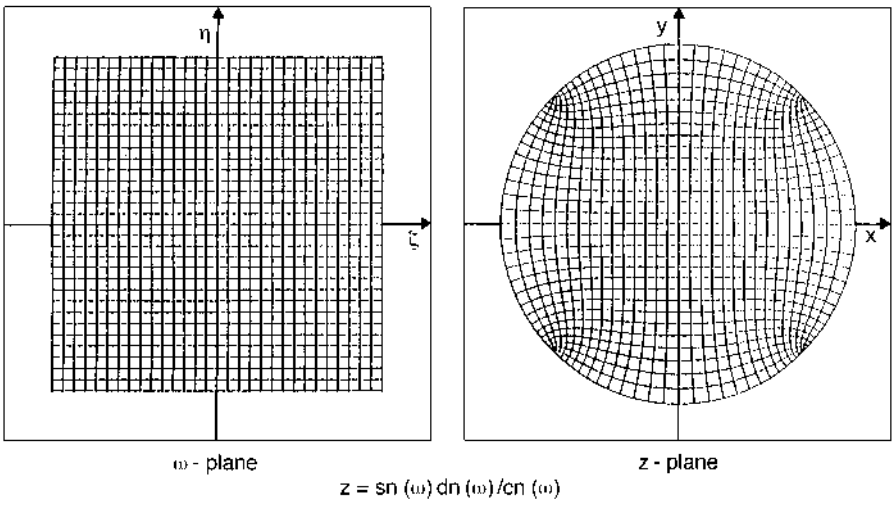

Figure 4.
Grid transformation

where $c = cn(\zeta, k)$, $c_1 = cn(\eta, k')$, $d = dn(\zeta, k)$, $d_1 = dn(\eta, k')$, $s = sn(\zeta, k)$ and $s_1 = sn(\eta, k')$ are Jacobian elliptic functions with real arguments. The complementary modulus $k' = \sqrt{(1-k^2)}$. For a square domain, it can be shown that $k'^2 = k^2 = 0.5$. Next, the elliptic functions are numerically evaluated using a descending Landen transformation (Bowman, 1961) and substitution in (33) and (34) gives the grid point coordinates (x, y).

The reverse transformation, $(x, y) \rightarrow (\zeta, \eta)$, involves an elaborate four-step procedure:

(1) The functions $s(\zeta, k)$ and $s_1(\eta, k')$ are pretabulated.

(2) Equation (31) is reduced to another system of non-linear, algebraic equations of the form

$$f(k, s, s_1, x) = 0 \tag{35}$$

$$g(k, s, s_1, y) = 0 \tag{36}$$

(3) Equations (35) and (36) are then solved simultaneously for s and s_1, for every x and y input, using a quasi Newton-Raphson numerical method.

(4) The coordinates (ζ, η) are recovered from the pretabulated functions $s(\zeta, k)$ and $s_1(\eta, k')$ via linear interpolation.

Velocity transformation

Let a fluid motion inside the square region of the ω-plane be given by the complex potential

$$W(\omega) = \phi + i\psi \tag{37}$$

where ϕ is the velocity potential and ψ is the streamfunction. Then at corresponding points z and ω, given by equation (31), W and therefore ϕ and ψ take the same values. Now, S' is a boundary and so a streamline, and therefore $\psi = C$, a constant, at all points of S'. Since S corresponds point by point with S', $\psi = C$ at all points of S. Therefore S is a streamline, in the motion given by (37) and (31) together, in the z-plane.

The actual form of the complex potential in terms of z would be obtained by eliminating ω between (31) and (37), but it is often preferable to look on z as a parameter and forgo the elimination. Thus, to find the fluid velocity at (x, y) in the z-plane corresponding with (ζ, η) in the ω-plane, we have

$$\frac{dW}{dz} = \frac{dW}{d\omega} \cdot \frac{d\omega}{dz} \tag{38}$$

The equivalent matrix form of equation (38) can be written as

$$\begin{bmatrix} u \\ v \end{bmatrix}_{(x,y)} = \begin{bmatrix} e_{11} & e_{12} \\ -e_{12} & e_{11} \end{bmatrix} \begin{bmatrix} u \\ v \end{bmatrix}_{(\zeta,\eta)} \tag{39}$$

where e_{11}, e_{22} are elements of the 2×2 matrix obtained from $d\omega/dz$.

Conversely, the fluid velocity at (ζ, η) in the ω-plane corresponding with the fluid velocity at (x, y) in the z-plane is given by

$$\frac{dW}{d\omega} = \frac{dW}{dz} \cdot \frac{dz}{d\omega} \tag{40}$$

or,

$$\begin{bmatrix} u \\ v \end{bmatrix}_{(\zeta,\eta)} = \begin{bmatrix} e_{11} & -e_{12} \\ e_{12} & e_{11} \end{bmatrix} \begin{bmatrix} u \\ v \end{bmatrix}_{(x,y)} \tag{41}$$

Notice that the matrix system in equation (41) is the inverse of that in equation (39). Off-grid point velocity calculation in either domain can be accomplished using an interpolation routine relevant to each grid system.

The validity of the conformal grid point and velocity transformation schemes discussed above were tested by comparing exact with numerical solutions. The grid point transformation $(\zeta, \eta) \rightarrow (x, y)$ was validated by attempting to recover the exact value (ζ, η) using the reverse transformation procedure discussed in the previous section. For the velocity field, the exact solutions obtained using the modified circle theorem (equation (28)) for a system of 105 vortices were compared with numerical solutions resulting from the transformation equation (39). The results of the error calculations are listed in Table III. As expected, the results show poor convergence at the corners of the domains because of the corner singularities inherent in the coordinate transformation scheme (see Figure 4). Outside of these singular regions excellent convergence was obtained. The corner singularities would prove to be a troublesome factor with regard to interpolation procedures.

To test the stability of the numerical prescription, the percent relative errors in both the tangential and radial components of velocity as a function of time were calculated. The results are illustrated in Figure 5. The increasing relative error for 0.05 sec $\leq t \leq$ 0.25 sec is essentially due to the loss of the organized vortex distribution which characterized the system initially (see Figure 2). The critical closeness of the vortex elements allows the motion of the vortices to be dominated by the effect of the singularity. Hald and Del Prete (1978) suggest a larger smoothing parameter in order to ensure better convergence results in the disorganized state. Beyond $t = 0.25$ sec the results indicate that the method is convergent to within 20 percent relative error and essentially stable.

Optimization of numerical parameters

Specifying threshold values for the following four relevant control parameters:

(1) m, mesh size;

(2) d_j, injector nozzle diameter;

(3) r_0, discrete-vortical element core radius;

(4) Δt, length of time step;

Errors	Grid point coordinates ζ	η	Velocity components u	v
Average absolute error	2.0397014E-07	1.4282386E-07	1.5206969E-01	1.4264177E-01
Maximum absolute error	1.3470206E-05	6.3128371E-06	3.4926014E+00	4.0869408E+00
Maximum relative error (%)	1.9993558E-02	1.0198522E-02	4.0998020E+07	9.2584425E+05
Root mean square error	6.8885259E-07	3.5780748E-07	3.3185267E-01	3.0976245E-01
Grid point location of maximum absolute error	(2,1), (2,61), (60,1), (60,61)	(1,3), (1,59), (61,59), (61,3)	(2,1), (2,61), (60,1), (60,61)	(1,3), (1,59), (61,59), (61,3)

Notes:

$$\text{Average absolute error} = \frac{\sum_{\substack{i=1\\j=1}}^{M} |p_E - p_N|}{M^2}$$

$$\text{Relative error (\%)} = \left[\frac{\sum_{\substack{i=1\\j=1}}^{M} (p_E - p_N)^2}{\sum_{\substack{i=1\\j=1}}^{M} p_E{}^2} \right]^{1/2} \times 100$$

$$\text{Root mean square error} = \left[\sum_{\substack{i=1\\j=1}}^{M} (p_E - p_N)^2 / M^2 \right]^{1/2}$$

where p is the parameter of interest and the subscripts E and N imply exact and numerical respectively

Table III.
Grid point and velocity transformation errors

the proper choice of a vortex core smoothing function $G_{ij}(z_i - z_j)$ and a numerical filter function φ will produce a discrete-vortical element calculation which describes a real flow. If the evolution of the important features of the real flow are to be predicted, then an appreciation for the interplay between these control parameters must be developed.

For details concerning the accuracy or consistency of the vortex core smoothing $G_{ij}(z_i - z_j)$, equation (12), see Hald and Del Prete (1978) and for considerations leading to the choice of Couet's filter function φ, equation (14), see (Ebiana and Bartholomew, 1996). Error estimates guiding the choice of m, d_j, r_0 and Δt are considered in this section.

Mesh size, m

Because the VIC formulation incorporates the streamfunction-vorticity finite-difference scheme, the question of grid resolution must be addressed. The accuracy of a finite difference scheme depends on the scale of the grid spacing (mesh size) relative to the scale of the exact solution or features of the real flow

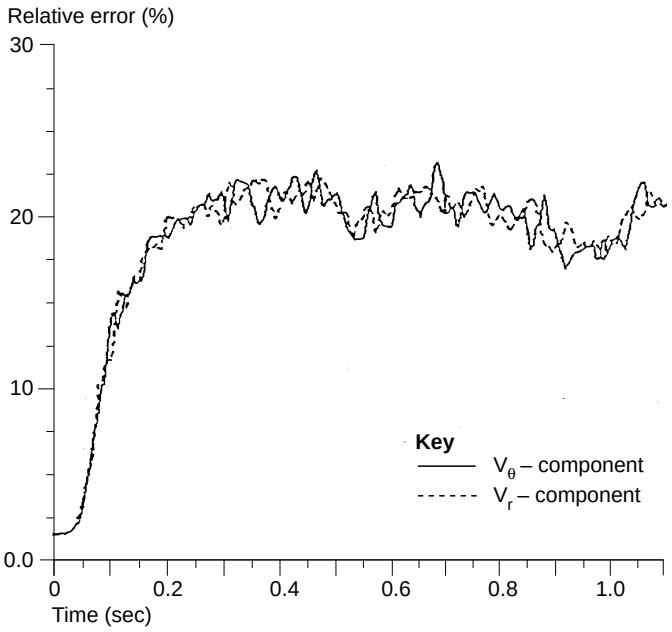

Figure 5.
Relative errors in V_r and V_θ versus time

which is being approximated numerically. To obtain a meaningful solution, the mesh size must be small enough to resolve the flow adequately. Theoretically, convergence of the numerical solution with exact solution should occur as the mesh size tends to zero.

The choice of the mesh size m used in this study is based on a comparison of the percent relative errors (computed as a function of the mesh size) in the grid point streamfunction values:

$$\text{Relative error (\%)} = \left[\frac{\sum_{i=1}^{M} \sum_{j=1}^{M} (\psi_E - \psi_N)^2 \cdot m^2}{\sum_{i=1}^{M} \sum_{j=1}^{M} \psi_E^2 \cdot m^2} \right]^{1/2} \times 100 \quad (42)$$

The numerical streamfunction, ψ_N, is computed via the VIC algorithm while the exact streamfunction, ψ_E, is obtained using equation (26).

Two tests were performed. The first compared the errors in the streamfunction field induced by a single discrete-vortical element of strength $\kappa = 1.0$, placed centrally in the computational grid. The second examined the effect of a system of 105 discrete vortices ($0.0 < \kappa < 1.06$) initialized in accordance with the point vortex initialization scheme. Plots of the percent relative errors for the various choices of grid sizes are presented in Figure 6. The plots confirm the theoretical predictions that the numerical approximation

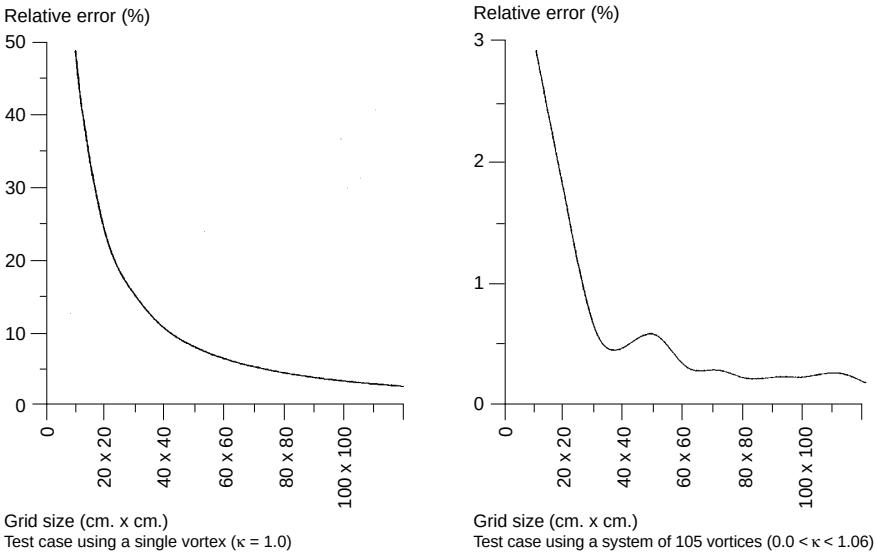

Figure 6.
Relative error between exact and numerical streamfunction values in the square domain using a single vortex and a system of 105 vortices

will converge to the exact solution as the mesh size tends to zero. This tendency is much more gradual for the second test case, especially for grid sizes within the range 60×60cm to 120×120cm. The choice of grid size anywhere in this range will produce comparable errors. From the practical standpoint of computational time and storage, a modest 60×60cm grid size (m = 0.0625cm) corresponding to 3,721 computational grid points was decided upon. The indicated relative error for this grid size is approximately 6 percent for the single vortex test case and 0.3 percent for the system of 105 vortices. The peak-to-peak variation observed in the second test suggests some interactions between neighboring vortices. These interactions act to reduce the relative error by as much as a factor of 20 when compared with the result for the single vortex test case. One should note that in practice, computations will rarely deal with an isolated vortex. Instead, a collection of vortices will be used to model a vortical region. Thus for the chosen mesh size, convergence is assured to a reasonable degree.

Injector nozzle diameter, d_j

No particular emphasis was placed in regard to the details of the injector nozzle design as these are not germane to the overall objective of this study. An optimization scheme for the injector nozzle diameter was not feasible in the absence of an exact jet flow solution. It is known, however, that for appropriate resolution of the jet features, the mesh size should be comparable to or smaller than the injector nozzle diameter. An injector nozzle diameter d_j (see Figure 1) equivalent to the mesh size m was deemed satisfactory for this study.

Vortex core radius, r_0

The application of the Green's function formulation requires the use of a vortex core radius to smooth the singularities. However, there is considerable difference of opinion in the literature as to the optimal smoothing parameter, r_0. Chorin and Bernard (1973) have observed that the results of their computations are insensitive to the exact details of the smoothing. On the other hand, Millinazzo and Saffman (1978) believe that the cut-off radius, r_0, should be as small as possible and used $\beta/50$, where β is the average distance between vortices. Hald and Del Prete (1978) have proven that the optimum cut-off depends upon the smoothness of the flow under consideration, and that for smooth flows, as the number of vortices increases, r_0 should be of order $\beta^{2/3}$. This implies that r_0 tends to zero more slowly than β; that is, there must be an ever increasing overlap of the circular vortices in order to maintain high accuracy in approximating a continuum of vorticity. This is natural, since as the vortices become packed closer together, the effect of the singularity in the fundamental solution of the Poisson equation, equation (8), becomes more pronounced and requires ever greater smoothing.

In light of the disagreement in the literature over what constitutes an acceptable value for the vortex core cut-off r_0, an empirical procedure has been devised in this study to optimize r_0. Since the vortex core radius r_0 is needed to smooth the singularities in the Milne Thomson's exact solution scheme and the VIC numerical solution scheme is independent of r_0, the procedure seeks to vary r_0 and compare the exact and numerical grid point solutions for the tangential component of velocity induced by a single discrete-vortical element of arbitrary strength $\kappa = 2\pi$ in the circular domain. The numerical solution was initiated in the square domain followed by the transformation techniques (discussed earlier) which provide the corresponding solution in the circular domain. For each arbitrarily chosen r_0, the percent relative error was measured as

$$\text{Relative error (\%)} = \left| \frac{\sum_{i=1}^{M} \sum_{j=1} [(V_\theta)_E - (V_\theta)_N]}{\sum_{i=1}^{M} \sum_{j=1} (V_\theta)_E} \right| \times 100 \quad (43)$$

The parameters $(V_\theta)_E$ and $(V_\theta)_N$ are the exact and numerical tangential velocities respectively. A value for r_0 that yielded the smallest error was considered the optimal choice for r_0 for use in this study.

Two tests cases were considered. In the first test, the vortex was located at the grid point in the middle of the square domain for symmetry. In the second test, the vortex was located at the center of one of the four cells surrounding the centrally located grid point. In each case, an equivalent vortex location in the circular domain was used for computing the exact solution. The results of the calculations for all grid points and for all grid points "sufficiently removed from the vortex singularity" are shown in Table IV. Note that the criterion

	Point vortex at grid point				
		For all grid points		For all grid points > 2.0m	
	Cutoff value	Minimum	Maximum	Minimum	Maximum
	…	…	…	…	…
	…	…	…	…	…
	…	…	…	…	…
	0.030	0.0000000E+00	3.3103230E+01	0.0000000E+00	8.2269478E+00
	0.031	0.0000000E+00	3.3123978E+01	0.0000000E+00	8.2309284E+00
	0.032	0.0000000E+00	3.3041328E+01	0.0000000E+00	8.2384529E+00
	0.033	0.0000000E+00	3.2821266E+01	0.0000000E+00	8.2486515E+00
	0.034	0.0000000E+00	3.2506222E+01	0.0000000E+00	8.2618771E+00
	0.035	0.0000000E+00	3.2149502E+01	0.0000000E+00	8.2778234E+00
→	0.036	0.0000000E+00	→ 3.1954117E+01	0.0000000E+00	8.2969713E+00
	0.037	0.0000000E+00	3.2173676E+01	0.0000000E+00	8.3195601E+00
	0.038	0.0000000E+00	3.2553860E+01	0.0000000E+00	8.3456974E+00
	0.039	0.0000000E+00	3.3207455E+01	0.0000000E+00	8.3754749E+00
	0.040	0.0000000E+00	3.3617626E+01	0.0000000E+00	8.4087601E+00
	0.041	0.0000000E+00	3.4297836E+01	0.0000000E+00	8.4481955E+00
	0.042	0.0000000E+00	3.5085903E+01	0.0000000E+00	8.4927826E+00
	…	…	…	…	…
	…	…	…	…	…
	…	…	…	…	…

	Point vortex at cell center				
		For all grid points		For all grid points > 1.5m	
	Cutoff value	Minimum	Maximum	Minimum	Maximum
	…	…	…	…	…
	…	…	…	…	…
	…	…	…	…	…
	0.043	0.0000000E+00	2.8972696E+01	0.0000000E+00	4.5753188E+00
	0.043	0.0000000E+00	2.7691328E+01	0.0000000E+00	4.5920501E+00
	0.044	0.0000000E+00	2.6544624E+01	0.0000000E+00	4.6130338E+00
	0.045	0.0000000E+00	2.5605698E+01	0.0000000E+00	4.6367159E+00
	0.046	0.0000000E+00	2.4890265E+01	0.0000000E+00	4.6635318E+00
	0.047	0.0000000E+00	2.4483385E+01	0.0000000E+00	4.6949511E+00
→	0.048	0.0000000E+00	→ 2.4455280E+01	0.0000000E+00	4.7295132E+00
	0.049	0.0000000E+00	2.5077896E+01	0.0000000E+00	4.7691174E+00
	0.050	0.0000000E+00	2.6744957E+01	0.0000000E+00	4.8136029E+00
	0.051	0.0000000E+00	2.8853853E+01	0.0000000E+00	4.8622284E+00
	0.052	0.0000000E+00	3.1229172E+01	0.0000000E+00	4.9168506E+00
	0.053	0.0000000E+00	3.4065449E+01	0.0000000E+00	4.9761343E+00
	0.054	0.0000000E+00	3.8109451E+01	0.0000000E+00	5.0421910E+00
	…	…	…	…	…
	…	…	…	…	…
	…	…	…	…	…

Note:
Mesh size = $m \times m$, m = 0.0625cm. Grid size = 60×60. Test grid size = 50×50, $\kappa = 1.0$

Table IV.
Comparison of the absolute value of the relative error (%) estimates between the modified exact and numerical tangential velocity values at grid points

"sufficiently removed from vortex singularity" is assured for grid points greater than two mesh lengths from a vortex located at a grid point and for grid points greater than one and a half mesh lengths from a vortex located at a cell center. When all grid points are considered the maximum error was observed to be minimum at $r_0 = 0.036$ for grid point location and $r_0 = 0.048$ for cell center location. For grid points "sufficiently removed from the vortex singularity", the trend, which is in line with expectation, suggests that convergence would occur in the limit as r_0 tends to zero. At equivalent r_0, the maximum errors were lower, as anticipated, for grid points "sufficiently removed from vortex singularity" than for all grid points by less than factors of four and six for grid point and cell center locations, respectively. The minimum relative error was zero for each consideration in both test cases. From the foregoing analysis, it was deemed reasonable to use an average value of $r_0 = 0.042$ for all vortex locations since the associated errors are comparable.

Time step, Δt

A general guideline for choosing a value for Δt is not discussed in the literature. An upper bound for Δt is usually given by the Courant condition $|V_{max}|(\Delta t/2) \leq m$. In this study, the value of the time step Δt is optimized by observing the trajectory of a single discrete-vortical element in the circular domain. Theoretically, it is expected that the vortex, whose motion is induced by its own velocity field, would trace a circle in one complete revolution. An error results if the initial radial position r_i of the vortex differs from the final radial position r_f after a complete revolution. Several tests were performed using a vortex of strength $\kappa = 2\pi$. For each chosen radial location, Δt is varied and the percent relative error after one complete revolution is calculated as

$$\text{Relative error (\%)} = \left| \frac{r_f - r_i}{r_i} \times 100 \right| \tag{44}$$

The results of these tests are shown in Figure 7. It is observed that the vortex motion in the central portion of the domain ($r^* < 0.6$), where $r^* = r/R$, is essentially insensitive to the time step and that convergence would occur as Δt tends to zero, which is again in line with theory. The time step $\Delta t = 0.001$ seconds was chosen sufficiently small, so that a decrease in the time step would not significantly affect the results.

To summarize, the threshold values for the control parameters and the numerical functions employed in this study are listed below:

Grid size, $M \times M$	$= 60 \times 60$cm.
Mesh size, $m \times m$	$= 0.0625 \times 0.0625$cm.
Injector nozzle diameter, d_j	= 0.0625 cm.
Vortex core cut-off, r_0	= 0.042 cm.
Time step, Δt	= 0.001 sec.

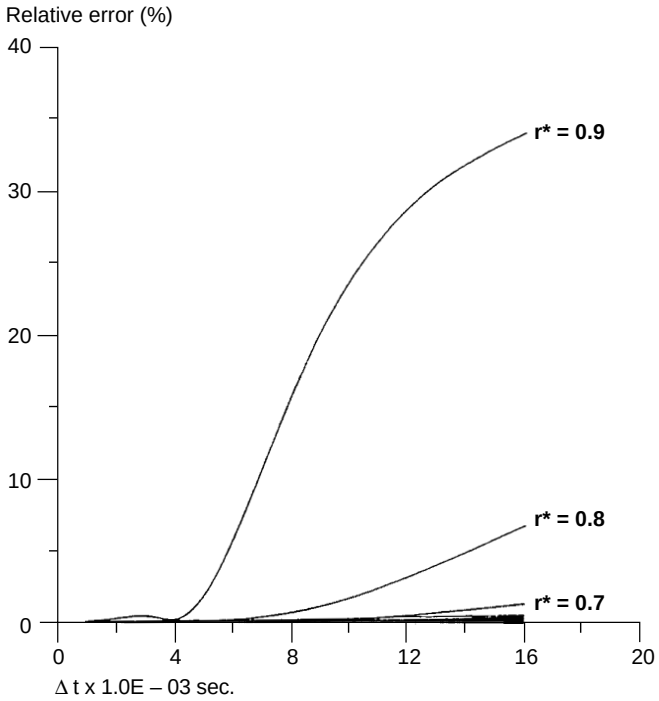

Figure 7.
Relative error between the initial and final positions of a discrete-vortical element after one complete revolution

Vortex core smoothing function:

$$G_{ij} = \begin{cases} \left[C_1\left(1 - \frac{|z_i - z_j|^3}{r_0^3}\right) - C_2\left(1 - \frac{|z_i - z_j|^2}{r_0^2}\right) + \log r_0\right]; & |z_i - z_j| \le r_0 \\ (z_i - z_j)^{-1} \qquad\qquad ; & |z_i - z_j| > r_0 \end{cases} \tag{12}$$

Couet's filter:

$$\varphi(\eta) = \begin{cases} \frac{1}{2}\left(\frac{3}{2} - |\eta|\right)^2 & ; \frac{1}{2} \le |\eta| \le \frac{3}{2} \\ \frac{3}{4} - \eta^2 & ; |\eta| \le \frac{1}{2} \\ 0 & ; \textit{otherwise} \end{cases} \tag{14}$$

Numerical simulations

The Fortran computer code for this study has the capability to track the jet vortices from the near wall injection point through their evolution in the interior of the cylinder. The jet algorithm was intended not as a rigorous model of the real jet behavior but more to explore by a numerical method how a jet flow might be expected to interact with a swirling cross flow.

The parameters influencing the interaction are the swirl strength S_θ (~ $\Sigma\kappa_j$), inlet jet velocity U_{in} and angle of injection θ_j. The angle of injection θ_j is set counter clockwise from the positive x-axis (see Figure 1). The inlet jet velocity U_{in} was determined by calculating, for each θ_j orientation, the distance per unit time step Δt covered by the vortex pair exiting the plane of the injector nozzle into the cylinder interior and just clearing the numerical boundary layer thickness δ_n. To simulate different initial swirl conditions, vortices were initialized as shown on Table II(b) to match Dyer's data (Table I) at the different times. Parametric studies were first conducted to identify the optimum conditions (S_θ, U_{in} and θ_j) for minimum complete diffusion time t^* defined as the time required for the jet vortices to completely fill the cylinder. The parameter t^* is therefore artificial. The criterion for complete diffusion was established by superimposing a square grid on the circular domain as shown in Figure 8 and ensuring that at least N_c vortices reside in each of the L square meshes or cells whose centers lie on the boundary or within the circular domain.

Fixed values of N_c = 2 and L = 32 were chosen from the point of view of computational economy and the effects of varying the inlet jet velocity U_{in} on the diffusion time t^* for fixed angle of injection θ_j and swirl strength S_θ were investigated to enable an appropriate choice of values for these parameters. The results of the parametric studies indicate that the optimum conditions are best represented by θ_j = 60°, S_θ=12.5cm.m/s and U_{in} = 210cm/s. Figure 9 illustrates test results for optimum θ_j = 60°. Notice the expected exponential decay trend for S_θ = 12.5cm.m/s.

From the series of parametric studies conducted, the following parameters were chosen for the numerical simulation: 6 × 6cm grid size (L = 32 cells), N_c = 2 vortices per cell, θ_j = 60°, S_θ = 12.5cm.m/s and U_{in} = 210.0cm/s. To help illustrate the nature of the flow in the cylinder, the results of the numerical experiments are presented for:

(1) swirling motion with no jet flow;

(2) jet flow with no swirling motion; and

(3) swirling motion with jet flow.

Vortex trajectory, velocity vector, streamline and velocity profile results for incremental time steps of 10ms up to when the cylinder wall is first hit and including when the cylinder is completely filled with jet vortices are illustrated.

Swirling motion with no jet flow

Figure 10 shows the geometric distribution for the system of 115 discrete vortices corresponding to S_θ = 12.5cm.m/s (see Table II(b)) and velocity vector representation of the swirling motion induced by these vortices as a function of time. Results are presented for selected times corresponding to short and long time errors illustrated in Figure 5. Representation of the velocity vector field on the non-uniform grid in the circular domain involves interpolation procedures implicit in the graphics routine used. This was not feasible due to the corner

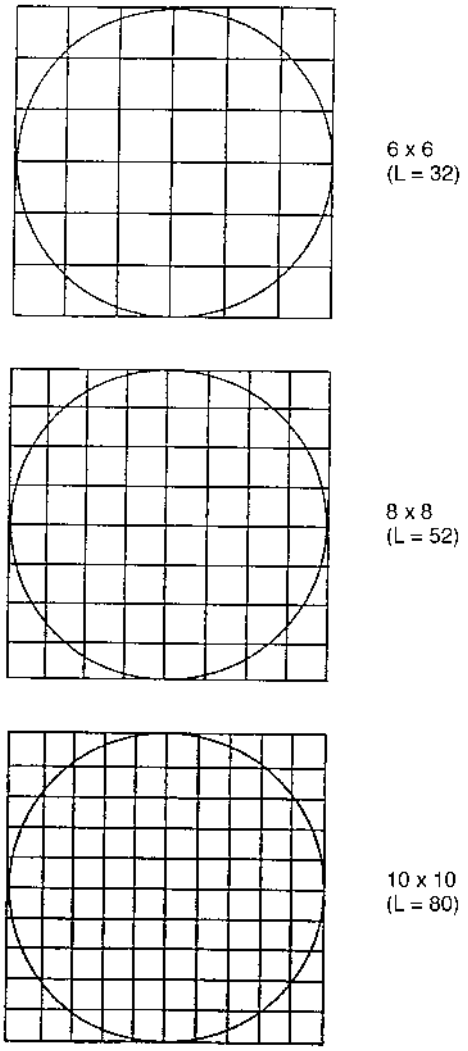

Figure 8.
Uniform grid squares superimposed on circular domain

singularities. To circumvent the interpolation problem a uniform 60×60cm. ($m \approx 0.017$cm) grid system was superimposed on the circular flow domain and the velocity information interpolated from the non-uniform grid system on to the uniform grid system. Vector information at every other grid point is illustrated. The magnitude of the vector at each grid point denotes the relative speed of the flow. The swirling fluid motion is characterized by a much slower moving, small central core region and a nearly constant tangential velocity for the bulk of the faster moving fluid. At the initial time, a high degree of swirling air-flow symmetry is achieved. As time progresses, the center-of-rotation of the swirling flow is offset from the cylinder axis resulting in the oscillatory motions

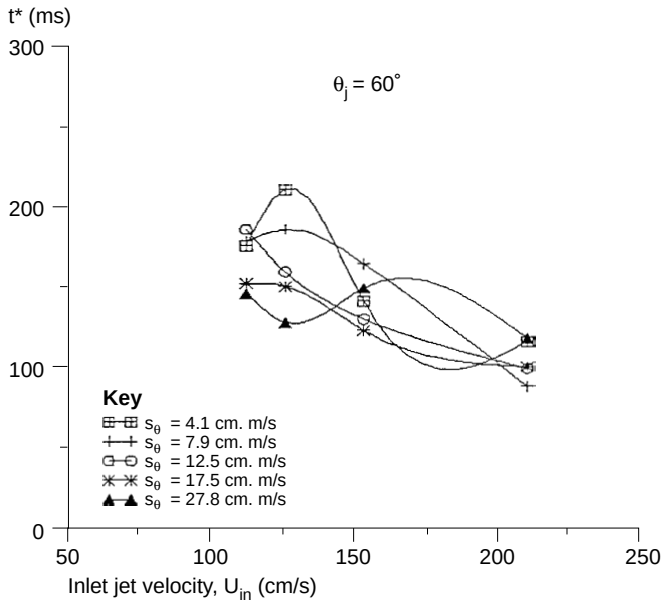

Figure 9.
Complete diffusion time as a function of the inlet jet velocity (number of cells L = 32, least number of jet vortices per cell N_c = 2)

most apparent near the center of the cylinder. The precession of the off-set center-of-rotation is gradually dissipated by the bulk of the fluid, the dissipation rate stabilizing somewhat beyond t = 200ms. It was observed that at times less than t = 50ms, corresponding to the relatively short, horizontal, lower left portion of Figure 5, the vortex distribution was still relatively organized. But at times greater than t = 50ms, the organized point distribution was lost. Figure 11 shows the corresponding radial and tangential velocity profiles. Predictions of theory are validated within 20 percent uncertainty.

Jet flow with no swirling motion

Figure 12 shows stages in the computed development of the jet vortices issuing at U_{in} = 210.0cm/s from an injector nozzle oriented at θ_j = 60° into a quiescent environment. It is observed that the dominant structure in the first few diameters of the jet after the onset of injection consists of an array of vortex pairs. A non-linear region followed where instabilities give rise to small clumps, or eddies which interact with each other and evolve into larger eddies as they move across the cylinder toward the wall. The vorticity coalescence results in the eddies loosing their identity. The occurrence and abruptness of the coalescence process depend on the irregularity in lateral spacing of the structures. A jet vortex first hits the wall at t = 29ms and its vorticity theoretically is destroyed when it is combined with its image vortex implying no flow through the wall. Note that the streamlines begin to distort as the vortices coalesce and the completely diffused situation at t = 271ms translates into the flow becoming more random, approaching a “turbulent” state. The closeness of streamlines are indicative of a high fluid velocity in that region.

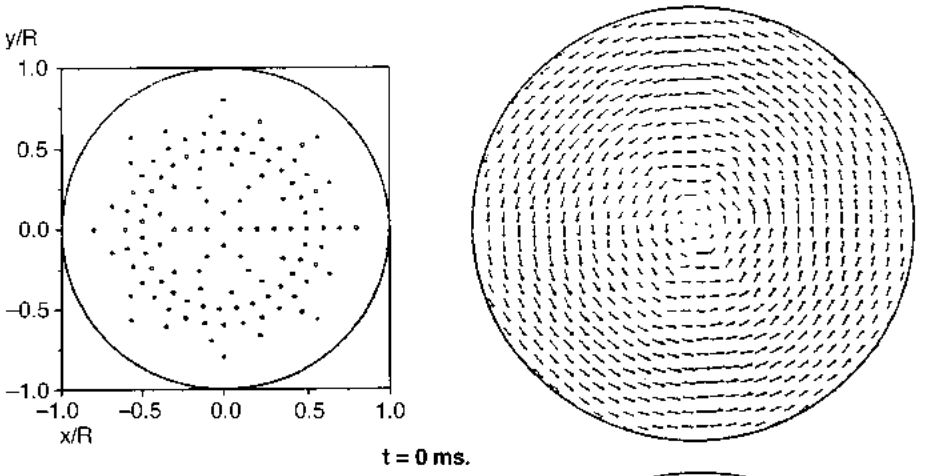

t = 0 ms.

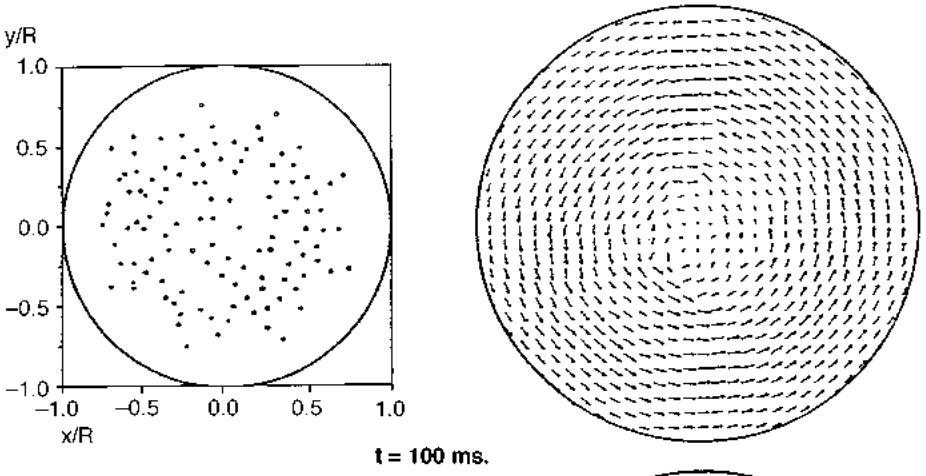

t = 100 ms.

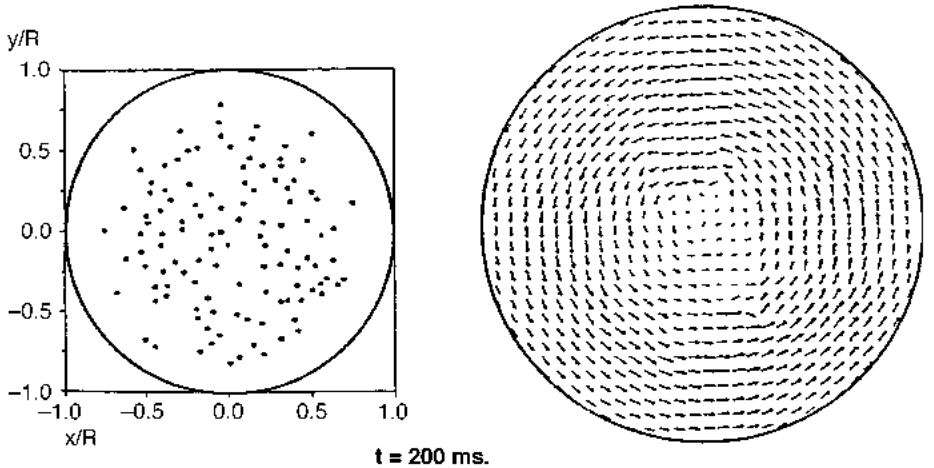

t = 200 ms.

(Continued)

Figure 10.
Geometric distribution of the system of 115 discrete vortices and velocity vector representation of the induced swirling motion

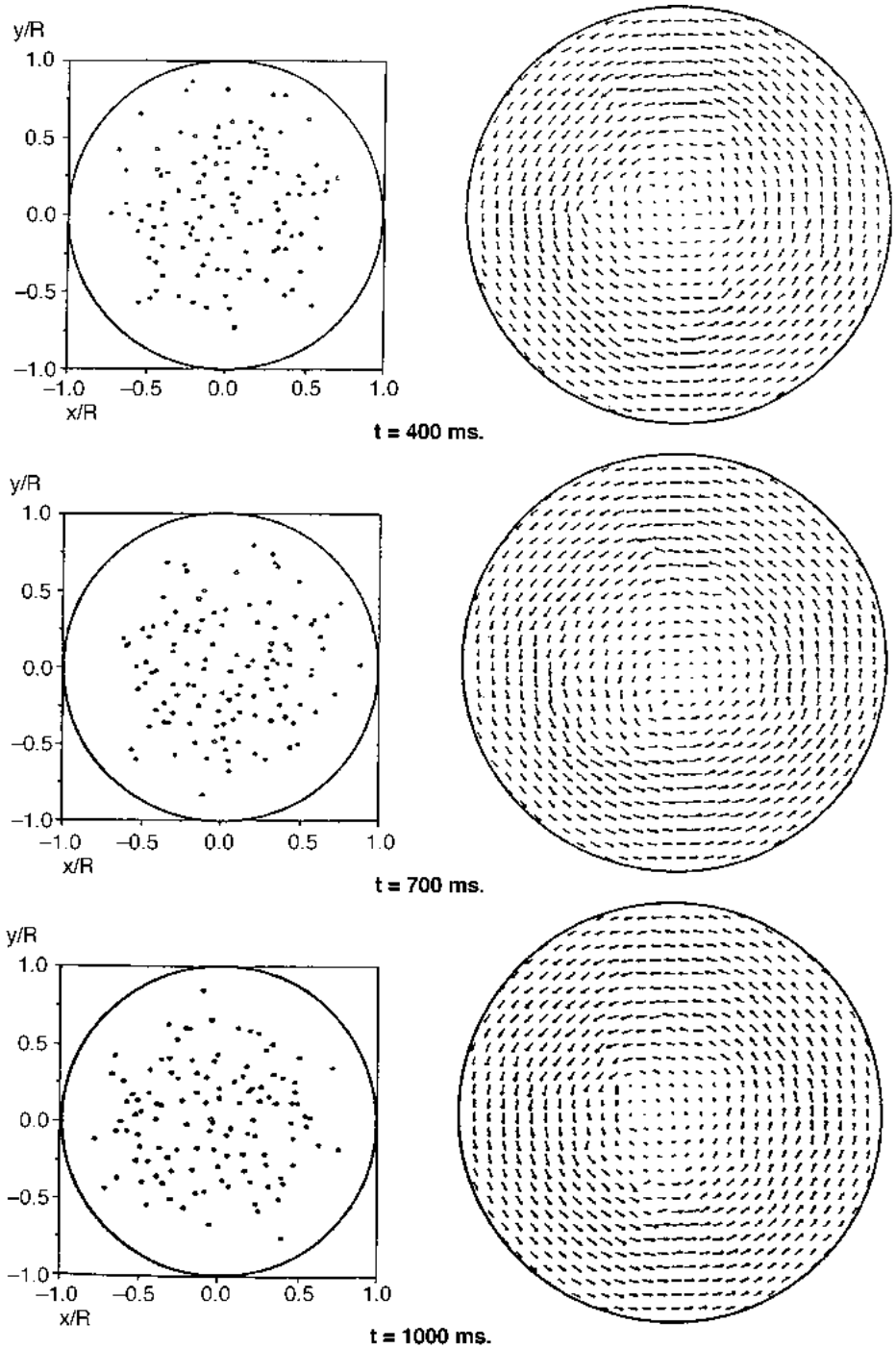
y/R
1.0
0.5
0.0
−0.5
−1.0
−1.0 −0.5 0.0 0.5 1.0
x/R
t = 400 ms.
y/R
1.0
0.5
0.0
−0.5
−1.0
−1.0 −0.5 0.0 0.5 1.0
x/R
t = 700 ms.
y/R
1.0
0.5
0.0
−0.5
−1.0
−1.0 −0.5 0.0 0.5 1.0
x/R
t = 1000 ms.

Figure 10.

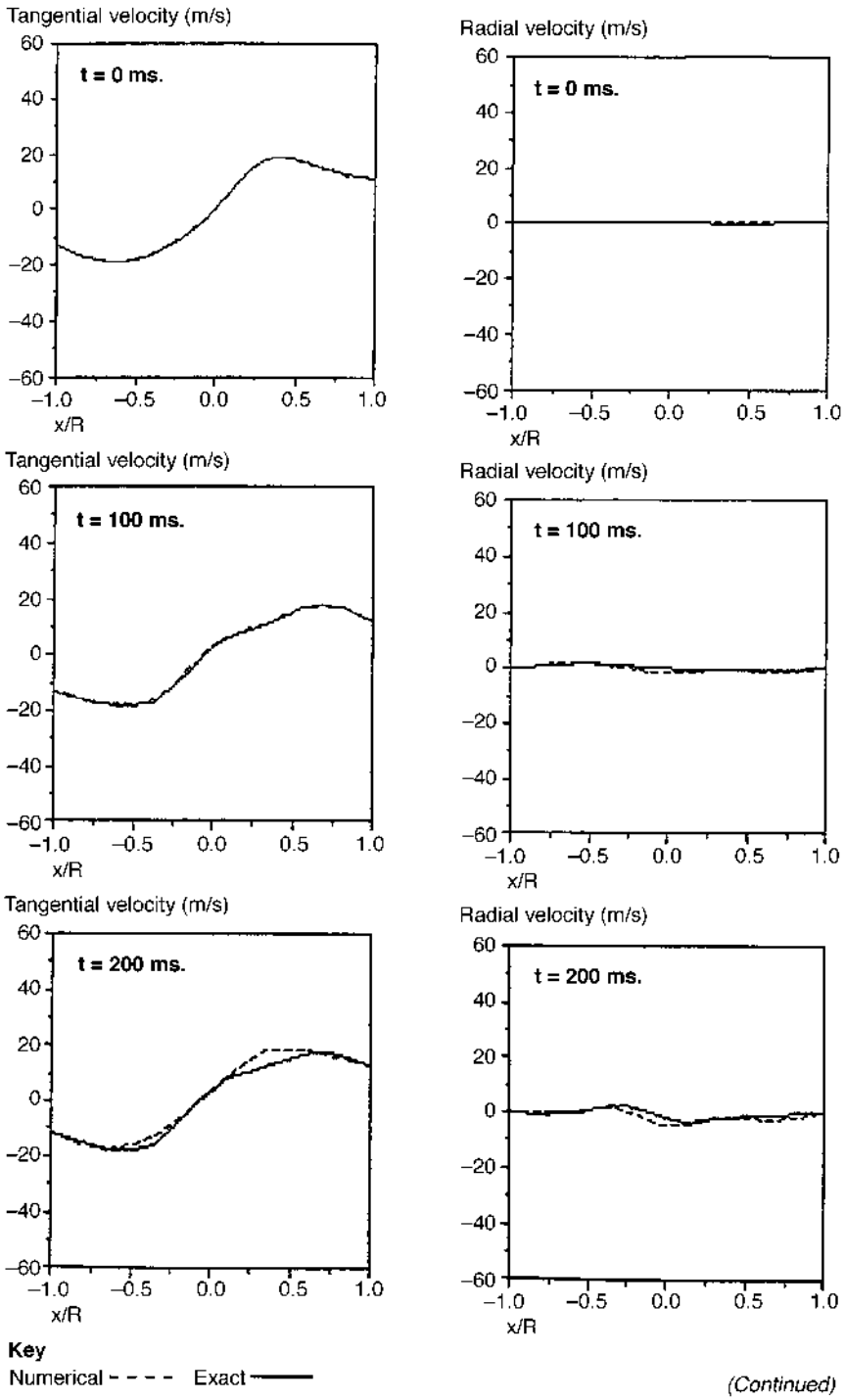

Figure 11.
Tangential and radial velocity profiles at discrete time steps

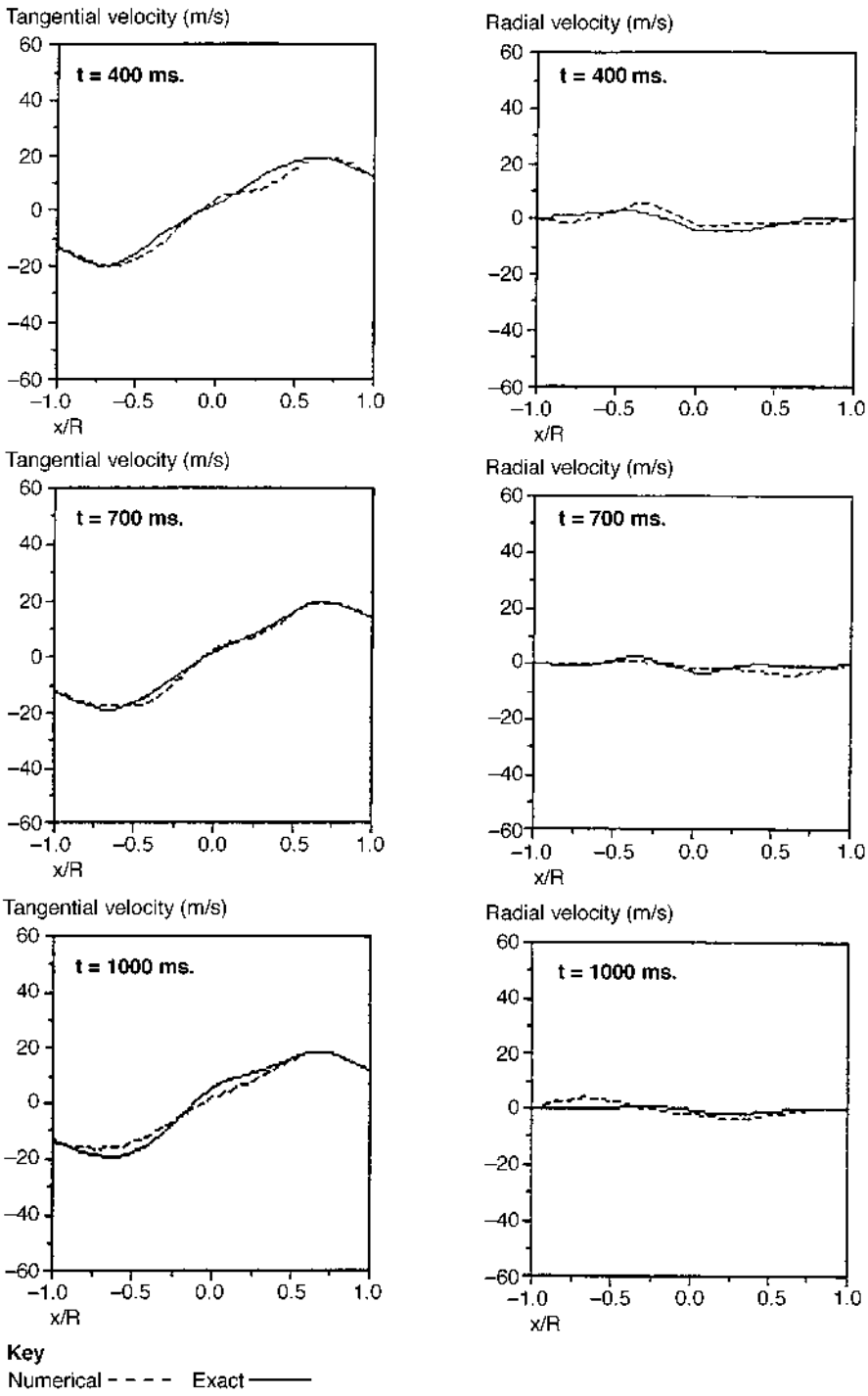
Tangential velocity (m/s)
t = 400 ms.
Radial velocity (m/s)
t = 400 ms.
Tangential velocity (m/s)
t = 700 ms.
Radial velocity (m/s)
t = 700 ms.
Tangential velocity (m/s)
t = 1000 ms.
Radial velocity (m/s)
t = 1000 ms.
60
40
20
0
-20
-40
-60
-1.0
-0.5
0.0
0.5
1.0
x/R
Key
Numerical - - - -
Exact ——

Figure 11.

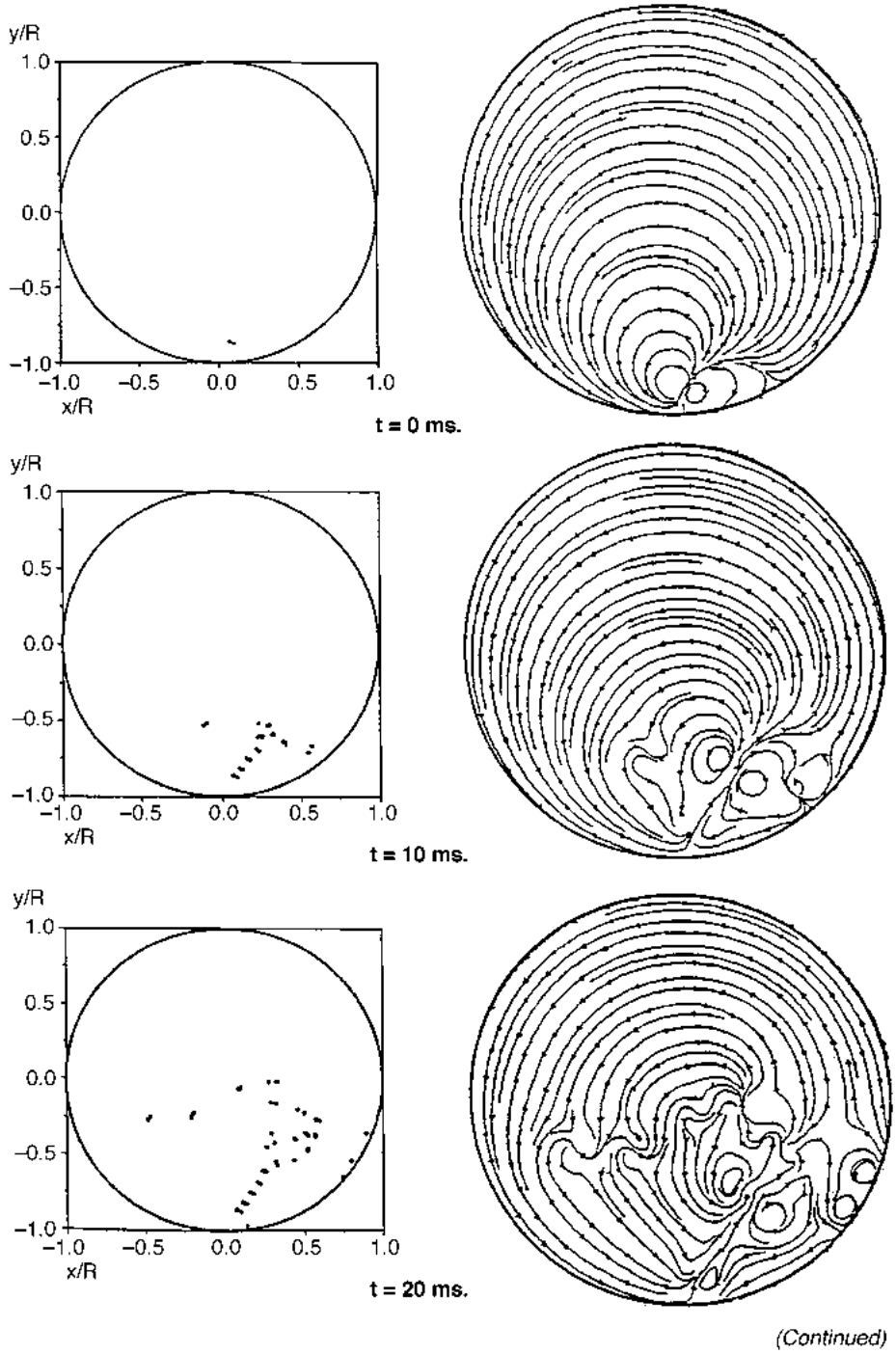

(Continued)

Figure 12.
Jet particle trajectory and streamlines as a function of time (without swirl). Injector of 60 degrees (counterclockwise from horizontal). U_{in} = 210.0m/s

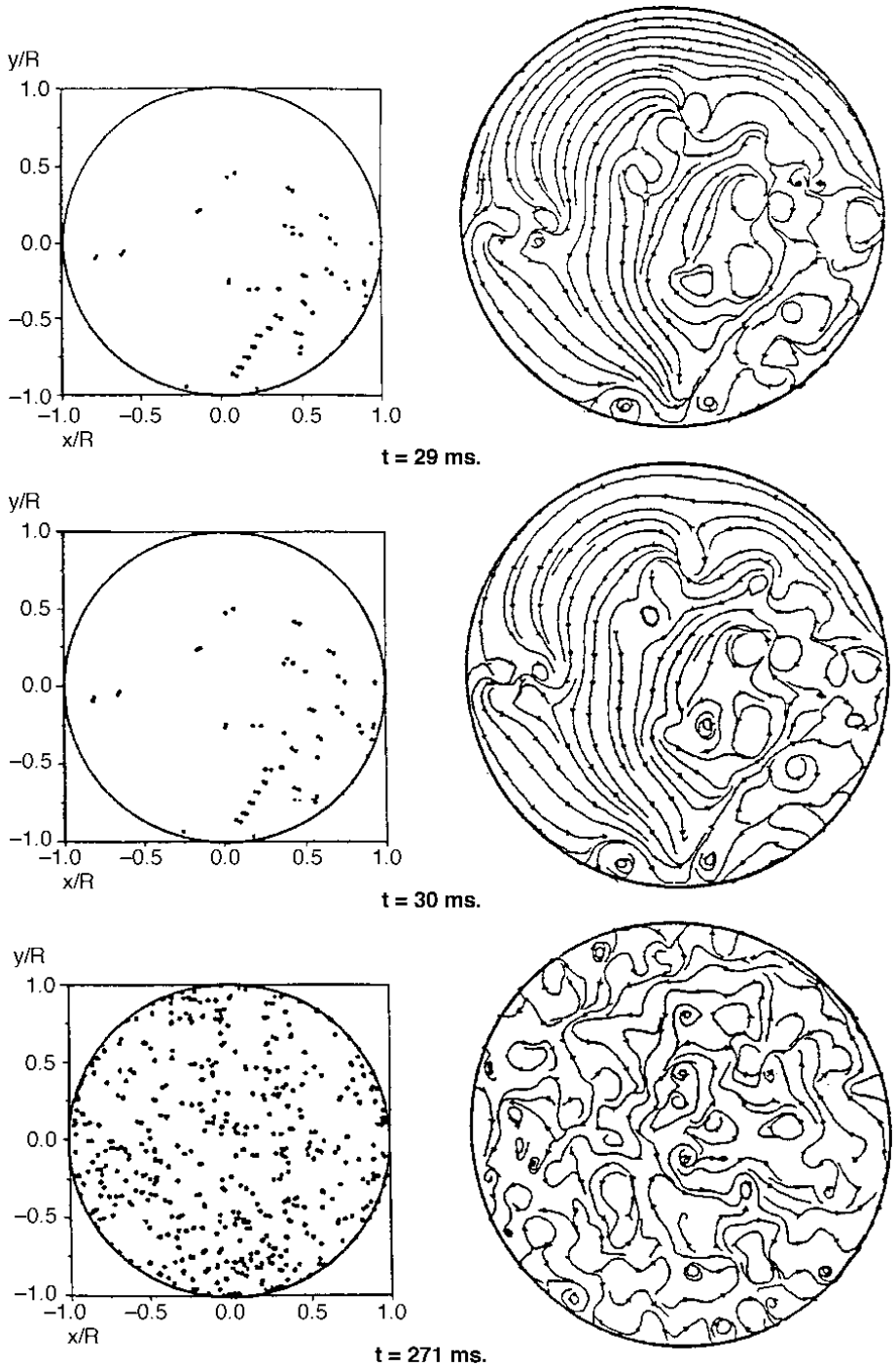
y/R
1.0
0.5
0.0
−0.5
−1.0
−1.0 −0.5 0.0 0.5 1.0
x/R
t = 29 ms.
y/R
1.0
0.5
0.0
−0.5
−1.0
−1.0 −0.5 0.0 0.5 1.0
x/R
t = 30 ms.
y/R
1.0
0.5
0.0
−0.5
−1.0
−1.0 −0.5 0.0 0.5 1.0
x/R
t = 271 ms.

Figure 12.

Swirling motion with jet flow

A global view of the interaction process is provided by Figure 13. Jet fluid at θ_j = 60° and U_{in} = 210.0cm/s issues into a swirling fluid of strength 12.5cm.m/s.

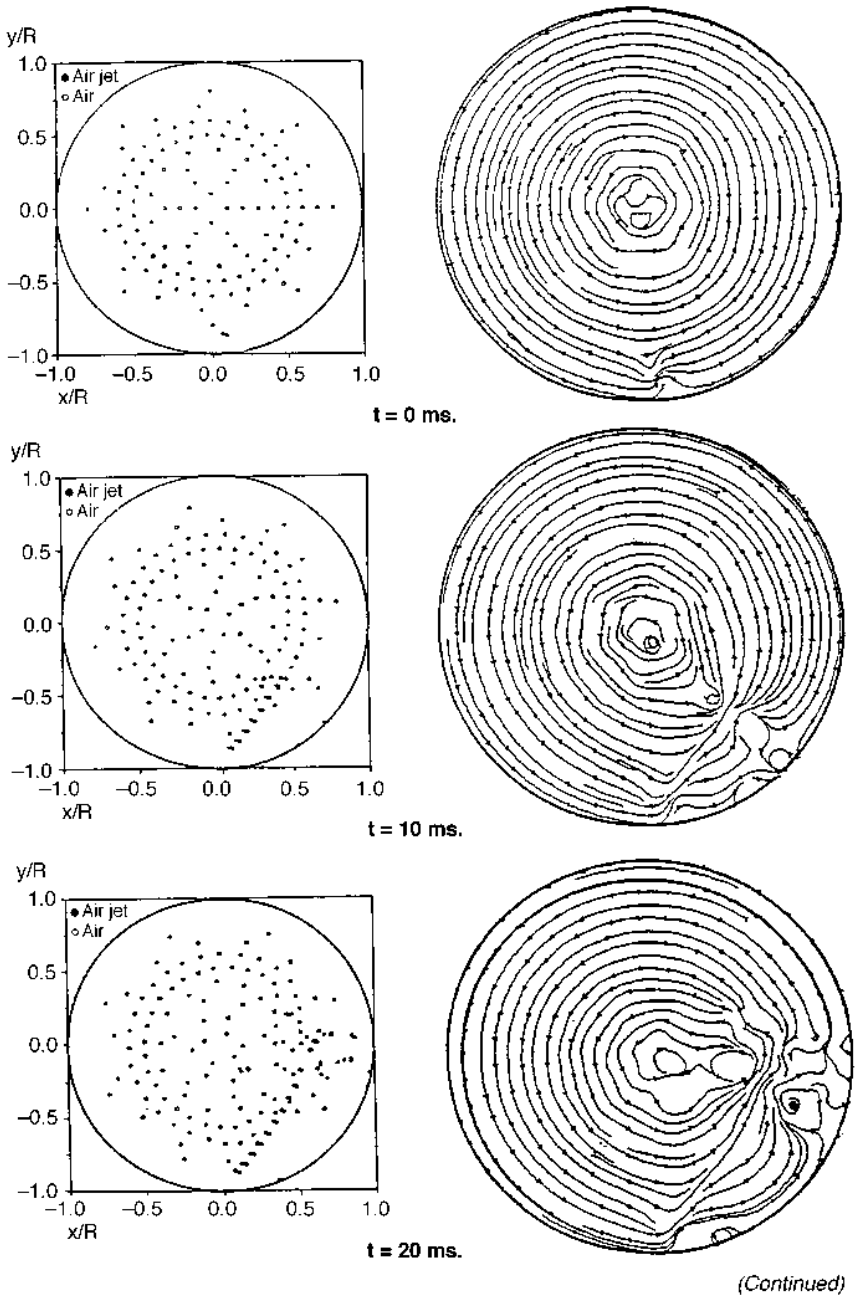

Figure 13. Cylinder/jet particle trajectory and streamlines as a function of time (swirl). Injector at 60 degrees (counterclockwise from horizontal). U_{in} = 210.0m/s

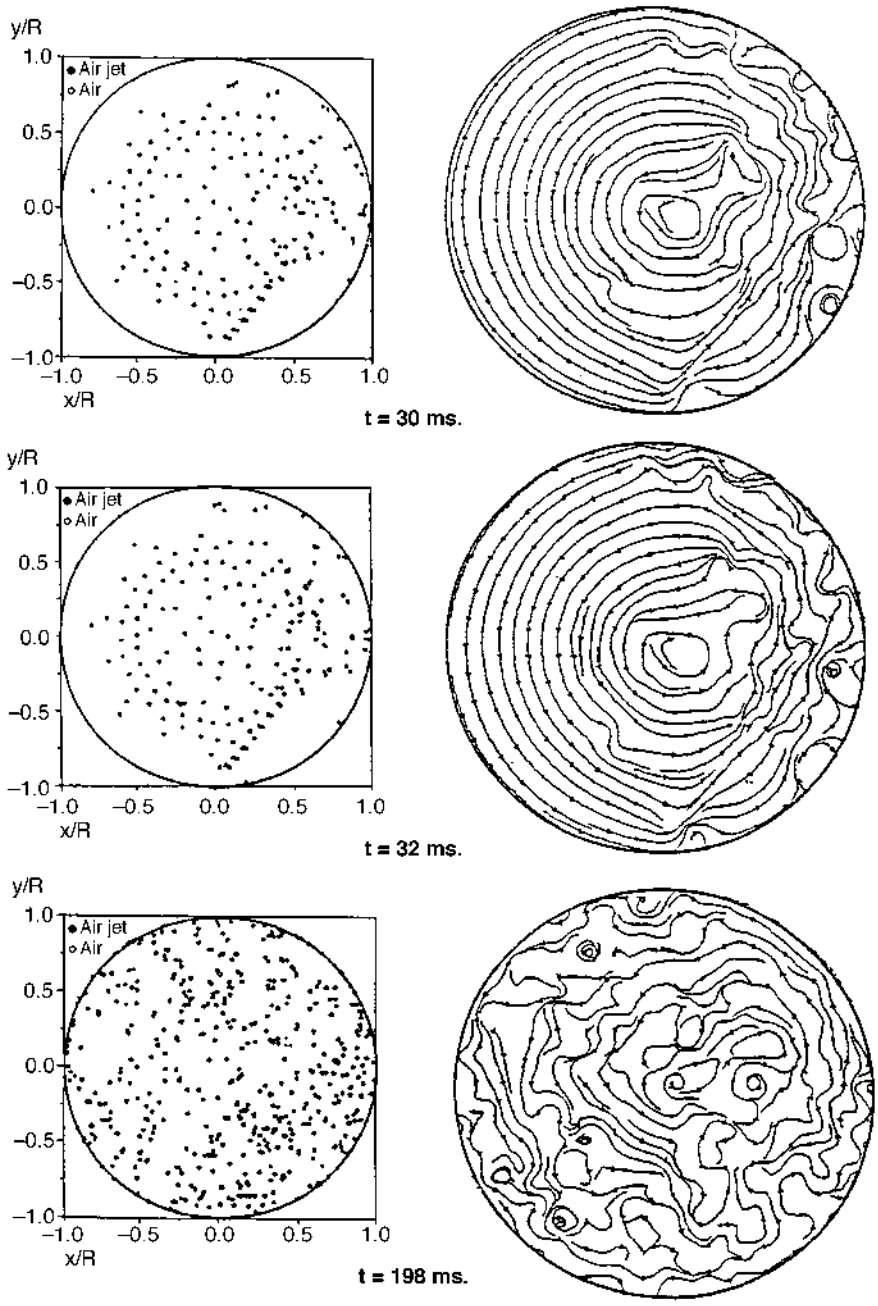

Figure 13.

As the jet enters the cylinder, it is deflected by the swirling flow and moves with it. Bulk diffusion results from the interactions of the swirl and jet vortices. If the force field of a vortex or cluster of neighboring vortices modeling the swirling

flow is stronger than that of a neighboring jet vortex or cluster, diffusion is inhibited. The higher swirl strength will only aid the transport of the jet vortices to the cylinder wall due to the centrifugal force acting on the jet vortices. On the other hand, diffusion is enhanced when a stronger jet overcomes the centrifugal force field and penetrates the flow. These contending phenomena are dictated by the relative strengths of neighboring vortices, and it is the net effect of these vortex interactions over time that results in the completely diffused situation. Notice the core of the jet is not significantly deflected by the air swirl as the jet passes across the cylinder toward the wall, implying that the jet vortices are stronger at those locations and are able to penetrate the centrifugal force field of the swirling flow. Soon after the jet penetrates the swirling flow, the identity of the jet tip is lost. Because of the absence of turbulent motion and molecular viscosity, the distribution of jet vortices (i.e. bulk diffusion) is determined primarily by the air swirl. It should be mentioned too that each swirl condition for these tests was obtained from a single realization of the vortex initialization scheme (see Table II(b)). Ideally each swirl condition should be obtained by averaging over several possible realizations.

The streamline patterns provide a qualitative appreciation of the interaction. The regions of great distortions of the streamline patterns are indicative of intense vortex interactions. The radial motion of the vortex particles is observed to be a small fraction of the tangential velocity due to centrifugal forces acting on them. This accounts for the jet vortices reaching the vicinity of the cylinder wall earlier (t = 10ms) than for the no swirl case (t = 20ms). Note that due to the influence of the swirling fluid motion, a jet vortex first hits the wall at t = 32ms later than for the no swirl case (t = 29ms). The fact that swirling flow does indeed aid the mixing process is seen in the faster complete diffusion time (t^* = 198ms) registered by this situation than for the no swirl case (t^* = 271ms).

To illustrate the flexibility of this numerical prescription, results for $\theta_j = 90°$ are presented in Figure A1 in the Appendix.

Further work

A discussion of the future directions of this research effort in terms of the physical modeling of all the processes encountered in the mixing problem is presented in this section.

Boundary-layer/vortical-structures interactions

Future research will consider the boundary layer region. The boundary layer region acts as a transition zone from the still fluid layer at the wall to the high speed flow in the interior. Since the viscous sublayer is thin compared to the radius of the cylinder, the Prandtl boundary layer equations for incompressible flow over a flat plate provide a reasonable description of the propagation of vorticity in this region. The computation of the flow field generated by discrete

vortical elements near solid boundaries has been shown by Chorin (1978) to have a slow rate of convergence. To improve the convergence rate in this region, Chorin introduced the vortex sheet algorithm to simulate a solution of Prandtl's boundary layer equations. The combined flow fields of the vortex algorithms for the interior and boundary layer regions must satisfy the no-slip condition for the velocity. By construction, the normal boundary condition $\mathbf{V}\cdot\mathbf{n} = 0$ on S (see Figure 1), is satisfied by both algorithms. However, the tangential boundary condition $\mathbf{V}\cdot\mathbf{s} = 0$, where $\mathbf{s}$ is a unit tangent vector on S, will require special attention. The vortex sheet algorithm was specially designed to impose this condition by mimicking the actual vorticity generation processes present on the wall.

Vortex sheets are surfaces parallel to solid walls across which the fluid velocity has a continuous normal component, but a discontinuous tangential component. The jump in the tangential velocity is the strength of the vortex sheet. A family of expressions similar to equations describing the movements of the discrete vortical elements in the interior domain, equation (13), can be derived for the vortex sheets. In this case, the Gaussianly distributed random variable η_j appears only in the y-component because Prandtl boundary layer equations take into account diffusion in the y direction only. In deriving these equations, an additional length scale, h, is introduced. This length scale is equal to the distance of separation between the test points on the solid boundary. Each time step, vortex sheets of appropriate strength are created to cancel the tangential slip velocity obtained from the vorticity distribution by integrating across the boundary layer thickness. The newly created sheets will move according to the vortex sheet algorithm. If they move too far from the wall, they are converted to interior vortical elements. If the interior vortical elements come too close to the wall they are returned to vortex sheets.

Intuitively, the vortex sheets move about in ideal flow together with a random y-component simulating viscous diffusion. Vortex sheets newly created to accommodate the boundary conditions diffuse out from the boundary by means of the random component and then get swept by the main flow. This mechanism then has most of the features a boundary layer should have. The parameters required to initiate the creation algorithm are the maximum allowable vortex element strength, γ_{max}, and the spacing between the test points on the wall, h.

It should be noted that continuous production of vorticity is not only due to the air jet but also to the vortex sheet production mechanism described above.

Mechanisms of vortical elements merging and dissipation

Vortex methods simulate the two-dimensional, incompressible Navier-Stokes equation by approximating the vorticity field ξ with a linear combination of Gaussian basis functions:

$$\xi(x) = \sum_{i=1}^{N} \frac{\kappa_i}{r_{0i}^2} \exp\left(-\frac{|x - x_i|^2}{4 r_{0i}^2}\right) \tag{43}$$

Each basis function or "vortex" has three parameters, (κ_i, x_i, r_{0i}), corresponding to its strength, position, which moves with the local velocity at that point, and width, respectively. Though the vortex positions can be likened to mesh points for gridded calculations, the geometry of the vortex positions is not built into the data structure as is the case for gridded computations. Thus, it is possible and even likely for many flow simulations for several computational elements to move toward each other and eventually overlap. In this case, the dynamics of the movement and diffusion of the overlapping vortex elements may coincide to a point where a single element with appropriate position, circulation, and width could express the same information.

It is important to distinguish between numerical merging and physical merging of Gaussian vortex elements. The distinction and the relationship to one another is crucial to understanding and designing merging algorithms. Numerical merging is merely replacing several basis functions with a single base function. Physical merging refers to the true vorticity dynamics when nearby patches or distributions of vorticity combine into a single element. Physical merging illustrates very clearly two competing but interconnected mechanisms in two-dimensional flow: on one hand, the generation of larger scales from smaller scales (two small vortices fuse to one large vortex), which in two-dimensional turbulence is responsible for the inverse energy cascade (Kraichnan and Montgomery, 1980); on the other hand, "induced" filamentation, the drawing out of long spiral arms as the vortices wrap around each other, is the real space agent of the enstrophy cascade (Meriless and Warn, 1975). In spite of its importance, our understanding why this merging takes place at all is still imperfect.

Clearly, the mechanisms of the vortical elements merging and dissipation, besides their physical significance, offer an important reduction in the computational effort for the numerical simulation. Future effort would be directed toward understanding and designing numerical merging algorithms in order to enhance computational efficiency. Since the computational elements must overlap considerably to control the induced error, a numerical merging event can be justified as a perturbation of the computational vorticity field. The dynamics of the discrete system will not play a role in the analysis because it suffices to consider only the instantaneous positions, widths, and circulations of vortices and not how they came to be in a given configuration.

Numerical merging will consist of replacing a collection of discrete vortical elements with a single element. From the N computational elements, a subset (κ_{ij}, x_{ij}, r_{0ij}) for $1 \le j \le n$ shall be merged into a single element. To understand the merging process, one must investigate the difference or error $e(x)$ in the vorticity fields before and after the merging event (Rossi, 1997):

$$e(x) = \frac{\kappa_0}{r_{00}^2}\left[\exp\left(-\frac{|x|^2}{4r_{00}^2}\right) - \sum_{i=1}^{n}\frac{\kappa_i r_{00}^2}{\kappa_0 r_{0i}^2}\exp\left(-\frac{|x - x_i|^2}{4r_{0i}^2}\right)\right] \quad (44)$$

Note that the postmerger element is labelled 0, the subindices *ij* having been dropped because only the n elements to be merged are of importance to the analysis. It is also assumed that all κ_i's ($i \leq i \leq n$) have the same sign. The goal is to choose efficiently a collection of vortices together with the parameters (κ_0, x_0, r_{00}) so that this error is small.

The extent to which chaotic motion is damped by finite core effects and viscosity is also an important issue that will be addressed in the future. Physically the idea of an element of vorticity stems from the diffusion of vorticity equation (6). Integrating this equation in space-time one gets:

$$\xi(x, t) = \frac{1}{\pi\epsilon^2}\int_{R^2}\xi_o(x')\, e^{-\frac{|x - x'|^2}{\epsilon^2}}\, dx' \quad (45)$$

where $\xi_0(x) = \xi(x, 0)$ is the initial distribution of vorticity and $\epsilon = 2(\nu t)^{1/2}$ is analogous to a viscous-core "cut-off" radius r_0 and it can be seen to evolve in time proportional to $(\nu t)^{1/2}$. Therefore after choosing the optimum numerical value of r_0 for the initial distribution of elements of vorticity (see discussion previous section) and the new ones introduced in the computational domain at each time step, then during the course of the simulation the value of r_0 should evolve in time according to the prescribed physical law. When $\epsilon(0)/\epsilon(t) \ll 1$ then dissipation of the vortical elements has occurred ("eddy" life-time exceeded).

Mixing

Since averaged quantities are primarily of interest in turbulent flows, use can be made of a formulation which models and solves the conservation equation, equation (15), for $P(\Psi; x, t)$, the averaged joint probability density function (PDF) of the scalars. The quantity $\Psi = (\psi_1, \psi_2, \ldots \psi_\sigma)$ is the σ-dimensional probability space corresponding to Φ. Henceforth, the argument $(\psi; x, t)$ is written (ψ), the dependence upon x and t being implied. The formal derivation of the transport equation for $P(\psi)$ is given in (Pope, 1979). The resulting equation is

$$\rho\left[\frac{\partial P(\Psi)}{\partial t} + \langle V_i\rangle\frac{\partial P(\Psi)}{\partial x_i}\right] + \frac{\partial \rho\langle v_i' p(\Psi)\rangle}{\partial x_i} = \frac{\partial}{\partial x_i}\left(\Gamma\frac{\partial P(\Psi)}{\partial x_i}\right) - \frac{\partial^2}{\partial\psi^2}\left\langle p(\Psi)\Gamma\frac{\partial\phi_\alpha}{\partial x_i}\frac{\partial\phi_\alpha}{\partial x_i}\right\rangle \quad (46)$$

where v_i' is the fluctuating component of V_i; that is $V_i = \langle V_i\rangle + v_i'$ and $p(\psi)$ is the instantaneous joint PDF, a random function due to the dependence of the

distribution of ϕ_α upon the initial conditions ϕ_α (x, 0), and the random forcing turbulence field $V(x, t)$. The angled brackets denote an averaged quantity. The physics of the evolution of scalar field undergoing turbulent and molecular mixing is embodied in the PDF transport equation (46).

It is interesting to observe the correspondences between the physically recognizable terms in equation (15) for the fluctuating scalar quantity ϕ and equation (46) for the averaged joint PDF $P(\psi)$. The convective term retains its structure in the PDF-equation but the turbulent convective contribution is added. The molecular transport term appears in the PDF-equation twofold : as a transport term in position space of the same structure as in the ϕ_α-equation, and as a transport term in probability space. Molecular transport in position space represents molecular diffusion while molecular transport in probability space represents mixing by molecular action. It is shown in (Pope, 1979) that the effect of the mixing term is to reduce the variance of $P(\psi)$ without affecting the mean.

Omitting the molecular diffusion terms, which are negligible at high Reynolds number, equation (46) reduces to

$$\rho\left[\frac{\partial P(\Psi)}{\partial t} + \langle V_i\rangle \frac{\partial P(\Psi)}{\partial x_i}\right] = -\frac{\partial \rho\langle v_i' p(\Psi)\rangle}{\partial x_i} - \frac{\partial^2}{\partial \psi^2}\langle p(\Psi)\Gamma \frac{\partial \phi_\alpha}{\partial x_i}\frac{\partial \phi_\alpha}{\partial x_i}\rangle \quad (47)$$

The transport equation in this form is not immediately soluble, because, whereas the term on the left is exact, the terms on the right, representing turbulent transport and molecular mixing respectively, are unknown and need to be modeled in order to close the transport equation for $P(\psi)$.

The closure of the turbulent transport and molecular mixing terms is the fundamental stumbling block to progress in probability formulation of turbulent scalar mixing. This is because turbulent mass transport or eddy diffusion is a complex process that is dependent on the scale and intensity of turbulence in the flow. Various models, have been proposed in the literature but a completely satisfactory model is yet to be demonstrated.

Pope's (1976) simple gradient diffusion model,

$$\frac{\partial \rho\langle v_i' p(\Psi)\rangle}{\partial x_i} = -\frac{\partial}{\partial x_i}\Gamma_t \frac{\partial P(\Psi)}{\partial x_i} \quad (48)$$

introducing the turbulent diffusion coefficient $\Gamma t(x, t)$, seems promising for the turbulent transport term and is better behaved for inert scalars and for large departures from Gaussianity and homogeneity.

For the molecular mixing term, a fluid particle Coalescence and Dispersion (C/D) model, which admits finite rate micromixing, was first proposed by Curl (1976). Curl derived an integro-differential equation for the rate of change of the

concentration probability density function, $p(c)$, which is a measure of the fraction of fluid particles having a concentration in the range "c" to "$c + \delta c$":

$$\frac{\partial}{\partial t}[p(c)] = \frac{1}{t_s}[p_o(c) - p(c)] - \frac{\partial}{\partial t}[xp(c)] + 8\beta\int_o^c p(c')\,p(2c-c')\,dc' - 2\beta p(c) \tag{49}$$

The terms on the right-hand side of the equation represent respectively the net inflow of concentration by advection, the disappearance of concentration by chemical reaction, the increase of concentration due to coalescence from all concentration ranges into the interval "c" to "$c + \delta c$" and the decrease of concentration by coalescence from the interval "c" to "$c + \delta c$" into other concentration ranges.

The model suggests a simple mechanism for the exchange of scalar concentration between initially segregated fluid particles that are fed continuously into a perfectly-stirred reactor. The fluid particles are pictured as undergoing independent pair collisions, representative of the molecular diffusion time scale. The model makes no attempt to describe the detailed dynamics of the turbulent flow but, instead, relies on a probability density function of concentration, itself dependent on empirically determined mixing frequency, β, to describe the non-uniformities in the flow. Pratt (1976) modeled the mixing term in the form

$$-\frac{\partial^2}{\partial\psi^2}\left\langle p(\Psi)\Gamma\frac{\partial\phi_\alpha}{\partial x_i}\frac{\partial\phi_\alpha}{\partial x_i}\right\rangle = -\beta P(\Psi) + 2^\alpha\beta\int P(\Psi+\Psi')\,P(\Psi-\Psi') \tag{50}$$

where $\beta(x, t)$ is the appropriate mixing frequency and ψ' is a dummy variable. The first term on the right-hand side models the disappearance of probability in the range $(\psi, \psi + d\psi)$ by coalescence with other scalar ranges. The integral represents the "generation" of probability in the range $(\psi, \psi + d\psi)$ by coalescence from all concentration ranges. This model is applicable to an arbitrary number of scalar quantities and can be expected to produce qualitatively correct results.

Given these modeling considerations, equation (47) can now be written as

$$\rho\frac{DP(\Psi)}{Dt} = \frac{\partial}{\partial x_i}\Gamma_t\frac{\partial P(\Psi)}{\partial x_i} - \beta P(\Psi) + 2^\alpha\beta\int P(\Psi+\Psi')\,P(\Psi-\Psi')\,d\Psi' \tag{51}$$

Equation (51) is to be solved in the finite domain D with boundary S. The problem is posed in the following terms : Given the initial joint PDF $P(\psi; x, 0)$, with two equally probable states (zero and unity) for $\phi_\alpha(x, t)$, $\alpha = 1, 2$, and the dynamic equation (51), obtain $P(\psi)$ for $t > 0$.

A numerical solution for $P(\psi)$ can be attempted by treating the simultaneous action of the advection, diffusion and mixing processes sequentially using Yanenko's (1971) operator splitting technique. The component equations are

$$\textit{Advection:} \qquad \frac{\partial P(\Psi)}{\partial t} + \langle V_i \rangle \frac{\partial P(\Psi)}{\partial x_i} = 0 \tag{52}$$

$$\textit{Eddy Diffusion:} \qquad \rho \frac{\partial P(\Psi)}{\partial t} = \frac{\partial}{\partial x_i} \left(\Gamma_t \frac{\partial P(\Psi)}{\partial x_i} \right) \tag{53}$$

$$\textit{Molecular Mixing:} \qquad \rho \frac{\partial P(\Psi)}{\partial t} = -\beta P(\Psi) + 2^n \beta \int P(\Psi+\Psi') P(\Psi-\Psi') d\Psi' \tag{54}$$

The advection of $P(\psi)$ by the mean flow (i.e. bulk diffusion) is obtained using the solutions from the analysis of the flow field discussed earlier. It is assumed that, to a first approximation, the motion of the injected scalar particle is identical to the motion of the Lagrangian point of fluid that would occupy the position of the particle if it were not there. That is, the conserved, passive, scalar field is advected by the fluid.

Turbulent diffusion of $P(\psi)$ can be approximated by adding turbulent velocity components to the droplet velocities. This requires that the turbulence intensity and length scales be specified. This point remains a formidable closure problem. The use of random walk in modeling turbulent diffusion was suggested by Chorin (1979) as a generalization of the random walk model used in his vortex sheet method for viscous diffusion.

Molecular mixing of $P(\psi)$ can be approximated using a Monte Carlo method, for the simulation of the coalescence-dispersion term. The Monte Carlo C/D scheme is a conceptually simple, stochastic fluid particle interaction model especially suited for mixing in discrete systems. An essential feature of the Monte Carlo computational technique is that at any location in the combustion chamber, the joint PDF is represented by an ensemble of fluid particles which are identified in terms of their individual thermodynamic states. The turbulent mixing process is described as a sequence of interactions between randomly chosen groups of n representative fluid particles which mix (with frequency β) completely with one another to form n new particles having an identical thermodynamic state. The simulation is allowed to continue until the ensemble statistics (mean and variance of properties) are observed to stabilize. Finally, the ensemble average and other statistics are obtained to represent the properties of interest.

The combination of the solutions for the advection, diffusion and mixing equations produces an approximation to the joint PDF solution for the turbulent mixing problem. Future research efforts will adapt the present computer code to incorporate these effects.

Lagrangian correlation coefficient

The Lagrangian correlation coefficient of the diffusive stochastic motion of the vortical elements has been ignored in the random walk correction as is the case in most relevant literature on random walk. The random walk correction at each time step was taken statistically independent of the random walk correction at previous time steps. It has been pointed out that statistical independence is a relatively *ad hoc* assumption and therefore physically wrong. Future work will attempt to incorporate the Lagrangian correlation coefficients in the simulation giving a physical statistical correlation of successive random walks along the lines of Brownian-motion ideas (Wang and Uhlenbeck, 1945).

Conclusion

This study sought to simulate the bulk diffusion of an inert scalar field due to the interaction of a jet flow and a swirling cross flow inside a two-dimensional cylinder. The numerical simulation is based on the concept of discrete-vortical element dynamics utilizing a Lagrangian-Eulerian scheme. The numerical results are compared to theoretical results for the velocity field and streamfunction obtained using the method of images (Figure A2 in the Appendix). Although the model provided herein is an idealized representation of a complex problem, predictions of theory have been well validated. Streamfunction values compare to within 6 percent for values induced by a single vortex and 0.3 percent for values induced by a system of 105 vortices. An estimate of the uncertainty in a given velocity measurement is about 20 percent. The swirling air motion and the features of a real jet are well simulated by the motion of a system of discrete vortices, adding confidence to the numerical prescription.

In meeting the present goal, a foundation was laid for a technique to initialize the vortex element distribution from a prescribed velocity data and useful insights have been provided on conformal transformation, parameter optimization and numerical code validation schemes.

There are many advantages that make a Lagrangian-Eulerian vorticity formulation appealing. The formulation in terms of vorticity removes pressure from the governing equations, thus reducing the number of variables which must be approximated. The compact support for vorticity permits vorticity-based methods to only concentrate on "relevant" areas whereas primitive variable formulations must resolve vorticity-free regions. The Lagrangian treatment eliminates the need to explicitly treat convective derivatives. The Eulerian grid in the VIC method allows the application in real space of an efficient numerical filter capable of subgrid resolution and leaving invariant the total circulation within each cell. The method generates a solution independent of the core radius of the discrete-vortical elements thereby avoiding the singularity inherent in the Green's function method. The VIC technique also offers a resolution of the problem of excessive computation time. The fast Fourier transform allows for the efficient solution of the Poisson's equation for the streamfunction in every time step of the simulation. Computational

economy is achieved because only $O(N)$ computer memory is required per time step, where N is the number of vortices, and the number of operations per time step in the FFT increases linearly with the number of vortex elements and mesh points.

Unlike other methods, discrete-vortical element methods are not limited at high Reynolds number of practical significance by the difficulty in distinguishing real from numerical diffusion. Convection and diffusion are handled by integral operators, which have inherent smoothing properties. This may be a great advantage over traditional techniques which are all based on differential operators. It should also be mentioned that vortex methods offer much promise as a technique for high-resolution simulation and that an additional benefit includes an increased understanding of vortex interactions at a level of sophistication consistent with the present needs of the design engineer.

Vortex methods are limited, however, like other methods, by the fact that effects not resolved cannot be seen, i.e. if there are not enough computational elements to represent a phenomenon, that phenomenon will not be observed. Boundary conditions are more difficult in a vorticity formulation as they are generally primitive variable constraints. The dependence of the method on an assumed non-deformable structure of the vortex makes analysis difficult since in reality vortices of finite size deform. Misrepresentation of the interaction of neighboring vortices can lead to a significant statistical error in any one realization of the solution. This obviously is the price that must be paid for the removal of numerically induced viscosity. In the VIC method, the vortex core cutoff is replaced, in effect, by the cell size which has an effect on the computations, e.g. the finite mode Fourier transform error, known as aliassing error. Also, since conformal transformation is a necessary requirement imposed by the choice of the VIC formulation, it is recommended that a transformation scheme free of singularities be chosen. It is necessary to eliminate such errors generated by the numerical procedure in order to obtain a smooth solution.

Finally, upon the inclusion of the physical modeling of all the processes discussed under “Further work”, the general structure and flexibility of the numerical scheme employed in this study make its extension to a two-phase flow a viable future objective.

References

Abernathy, F.H. and Kronauer, R.E. (1962), “The formation of vortex streets”, *Journal of Fluid Mechanics*, Vol. 13, p. 1.

Anderson, C. and Greengard, C. (1985), “On vortex methods”, *SIAM Journal on Numerical Analysis*, Vol. 22, pp. 413-40.

Ashurst, W.T. (1981), “Piston-cylinder fluid motion via vortex dynamics”, in Morel, T. *et. al.* (Eds), *Fluid Mechanics of Combustion Systems*, Fluid Engineering Division, ASME, Boulder, CO.

Beale, J.T. and Majda, A. (1982), “Vortex methods II: higher order accuracy in two and three dimensions”, *Mathematics of Computation*, Vol. 39, pp. 29-52.

Bowman, F. (1961), *Introduction to Elliptic Functions with Applications*, Dover Publications, Inc., New York, NY.

Chorin, A.J. (1973), "Numerical studies of slightly viscous flow", *Journal of Fluid Mechanics*, Vol. 57, pp. 785-96.

Chorin, A.J. (1978), "Vortex sheet approximation of boundary layers", *Journal of Computational Physics*, Vol. 27, pp. 428-42.

Chorin, A.J. (1979), "Numerical methods for use in combustion modeling", *Proceedings of the International Conference on Numerical Methods in Science and Engineering*, Versailles, France, pp. 229-36.

Chorin, A.J. and Bernard, P.S. (1973), "Discretization of a vortex sheet, with an example of roll-up", *Journal of Computational Physics*, Vol. 13, pp. 423-9.

Couet, B., Buneman, O. and Leonard, A. (1981), "Simulation of three-dimensional incompressible flows with vortex-in-cell methods", *Journal of Computational Physics*, Vol. 39, pp. 305-28.

Curl, R.L. (1976), "Dispersed phase mixing: I. theory and effects of simple reactors", *A.I.Ch.E.J.*, Vol. 78, p. 535.

Dyer, T.M. (1978), "Characterization of one- and two-dimensional homogeneous combustion phenomena in a constant volume bomb", Sandia National Labs, Report SAND78-8704.

Ebiana, A.B. and Bartholomew, R.W. (1996), "Design considerations for numerical filters used in vortex-in-cell algorithms", *Computers and Fluids*, Vol. 25 No. 1, pp. 61-75.

Hald, C. and Del Prete, V.M. (1978), "Convergence of vortex methods for Euler's equations", *Mathematics of Computation*, Vol. 32, pp. 791-809.

Koumoutsakos, P. and Shiels, D. (1996), "Simulations of viscous flow normal to an impulsively started and uniformly accelerated flat plate", *Journal of Fluid Mechanics*, Vol. 328, pp. 177-227.

Kraichnan, R.H. and Montgomery, D. (1980), "Two-dimensional turbulence", *Rep. Prog. Phys.*, Vol. 43, pp. 547-619.

Leonard, A. (1980), "Vortex methods for flow simulations", *Journal of Computational Physics*, Vol. 37, pp. 289-335.

Meneghini, J.R. and Bearman, P.W. (1995), "Numerical simulation of high amplitude oscillatory flow about a cylinder", *Journal of Fluids and Structures*, Academic Press Limited, Vol. 9, pp. 435-55.

Meriless, P.E. and Warn, H. (1975), "On energy and enstrophy exchange in two-dimensional non-divergent flow", *Journal of Fluid Mechanics*, Vol. 69, pp. 625-30.

Millinazzo, F. and Saffman, P.G. (1978), "The calculation of large Reynolds number two-dimensional flow using discrete vortices with random walk", *Journal of Fluid Mechanics*, Vol. 84, part 3, pp. 433-53.

Milne-Thomson, L.M. (1940), "Hydrodynamical images", *Proceedings of the Cambridge Philosophical Society*, Vol. 36, pp. 246-7.

Park, K.H., Metcalfe, R.W. and Hussain, F. (1994), "Role of coherent structures in an isothermally reacting mixing layer", *Phys. Fluids*, Vol. A6, pp. 885-902.

Pope, S.B. (1976), "The probability approach to the modeling of turbulent reacting flow", *Combustion and Flame*, Vol. 27, p. 299.

Pope, S.B. (1979), *Philos. Trans. R. Soc. London*, Ser. A291, p. 529.

Pratt, D.T (1976), "Mixing and chemical reaction in continuous combustion", *Prog. Energy Combustion Sci.*, Vol. 1, p. 73.

Rosenhead, L. (1931), *Proc. Royal Soc.*, Vol. A134, p. 170.

Rossi, L.F. (1997), "Merging computational elements in vortex simulations", *SIAM Journal on Scientific Computing*, Vol. 18, No. 4.

Schadow, K.C. (1989), "Large-scale coherent structures as drivers of combustion instability", *Combustion Science and Technology*, Vol. 64 No. 4-6, pp. 167-86.

Sung, H.J. (1994), "Discrete vortex simulation of pulsating flow behind a normal plate", *Journal of Fluids Engineering*, Vol. 116, pp. 862-9.

Takami, H. (1964), "Numerical experiment with discrete vortex approximation, with reference to the rolling up of a vortex sheet", *Dept. of Aero. and Astro.*, Stanford University, Report SUDAER 202.

Wang, M.C. and Uhlenbeck, G.E. (1945), "On the theory of the Brownian motion II", *Reviews of Modern Physics*, Vol. 17 Nos. 2 and 3.

Winckelmans, G.S. and Leonard, A. (1993), "Contributions to vortex particle methods for the computation of three-dimensional incompressible unsteady flows", *Journal of Computational Physics*, Vol. 109 No. 2, pp. 247-73.

Yanenko, N.N. (1971), *The Method of Fractional Steps*, Springer Verlag, New York, NY.

Further reading

Stratonovichm, R.L. (1963), *Topics in the Theory of Random Noise*, Vol. 1, Chapters 1 & 4, New York, NY.

Appendix. Derivation of the streamfunction ψ inside a finite rectangular domain using method of images

Notes: (1) Sign convention: counterclockwise is positive.
(2) $\omega = \zeta \pm i\eta$

Consider the η direction:

$$W(\omega) = -i\kappa\Big\{\underbrace{\ln[\omega-(\zeta_0+i\eta_0)]}_{\#1} - \underbrace{\ln[\omega-\{\zeta_0+i(2K-\eta_0)\}]}_{\#2} - \underbrace{\ln[\omega-(\zeta_0-i\eta_0)]}_{\#3} + \underbrace{\ln[\omega-\{\zeta_0+i(2K+\eta_0)\}]}_{\#4} + \underbrace{\ln[\omega-\{\zeta_0-i(2K-\eta_0)\}]}_{\#5} - \underbrace{\ln[\omega-\{\zeta_0+i(4K-\eta_0)\}]}_{\#6} - \underbrace{\ln[\omega-\{\zeta_0-i(2K+\eta_0)\}]}_{\#7} + \ldots\Big\}$$

$$= -i\kappa\{\ln(\omega-\omega_0) - \ln(\omega-\bar{\omega}_0-i2K) - \ln(\omega-\bar{\omega}_0) + \ln(\omega-\omega_0-i2K) + \ln(\omega-\omega_0+i2K) - \ln(\omega-\omega_0-i4K) - \ln(\omega-\bar{\omega}_0-i2K) + \ldots\}$$

$$= -i\kappa\{[\ln(\omega-\omega_0)+\ln(\omega-\omega_0-i2K)+\ln(\omega-\omega_0+i2K)+\ldots] - [\ln(\omega-\bar{\omega}_0)-\ln(\omega-\bar{\omega}_0-i2K)-\ln(\omega-\bar{\omega}_0+i2K)+\ldots]\}$$

$$= -i\kappa\left\{\sum_{n=-\infty}^{\infty}\ln[\omega-\omega_0+i2nK]-\sum_{n=-\infty}^{\infty}\ln[\omega-\bar{\omega}_0+i2nK]\right\}$$

$$= f(\omega)+\bar{f}(\omega) \tag{A.1}$$

where

$$f(\omega) = -i\kappa\sum_{n=-\infty}^{\infty}\ln[\omega-\omega_0+i2nK]$$

$$\bar{f}(\omega) = i\kappa\sum_{n=-\infty}^{\infty}\ln[\omega-\bar{\omega}_0+i2nK]$$

Now, consider $f(\omega)$:

$$f(\omega) = -i\kappa\ln\left\{(\omega-\omega_0)[(\omega-\omega_0)+i2K][(\omega-\omega_0)-i2K][(\omega-\omega_0)+i4K]+\ldots\right\}$$

$$= -i\kappa\ln\left\{(\omega-\omega_0)\prod_{n=1}^{\infty}[(\omega-\omega_0)^2+(2nK)^2]\right\}$$

$$= -i\kappa\ln\left[\frac{\pi(\omega-\omega_0)}{2K}\frac{2K}{\pi}\prod_{n=1}^{\infty}\left[1+\left\{\frac{(\omega-\omega_0)}{2nK}\right\}^2\right](2nK)^2\right]$$

$$= -i\kappa\left\{\ln\left[\frac{\pi(\omega-\omega_0)}{2K}\prod_{n=1}^{\infty}\left[1+\left\{\frac{(\omega-\omega_0)}{2nK}\right\}^2\right]\right]+\ln\left[\frac{2K}{\pi}\prod_{n=1}^{\infty}(2nK)^2\right]\right\}$$

$$= -i\kappa\left\{\ln\left[\sinh\left\{\frac{\pi(\omega-\omega_0)}{2K}\right\}\right]+\ln\left[\frac{2K}{\pi}\prod_{n=1}^{\infty}(2nK)^2\right]\right\}$$

$$= -i\kappa\ln\left[\sinh\left\{\frac{\pi(\omega-\omega_0)}{2K}\right\}\right]+C_1 \tag{A.2}$$

where

$$\sinh\left\{\frac{\pi(\omega-\omega_0)}{2K}\right\} = \left[\frac{\pi(\omega-\omega_0)}{2K}\prod_{n=1}^{\infty}\left[1+\left\{\frac{(\omega-\omega_0)}{2nK}\right\}^2\right]\right]$$

$$C_1 = -i\kappa\ln\left[\frac{2K}{\pi}\prod_{n=1}^{\infty}(2nK)^2\right]$$

Similarly, it can be shown that:

$$\bar{f}(\omega) = i\kappa\ln\left[\sinh\left\{\frac{\pi(\omega-\bar{\omega}_0)}{2K}\right\}\right]-C_1 \tag{A.3}$$

Substituting (A.2) and (A.3) in (A.1) gives:

$$W(\omega) = -i\kappa\left\{\ln\left[\sinh\left\{\frac{\pi(\omega-\omega_0)}{2K}\right\}\right] - \ln\left[\sinh\left\{\frac{\pi(\omega-\bar{\omega}_0)}{2K}\right\}\right]\right\}$$

$$= -i\kappa \ln\left[\sinh\left\{\frac{\pi(\omega-\omega_0)}{2K}\right\}\Big/\sinh\left\{\frac{\pi(\omega-\bar{\omega}_0)}{2K}\right\}\right]$$

$$= -i\kappa \ln\left[\frac{\sinh(\zeta_m+i\eta_m)}{\sinh(\zeta_m+i\eta_p)}\right]$$

$$= -i\kappa \ln\left[\frac{\sinh(\zeta_m)\cos(\eta_m) + i\cosh(\zeta_m)\sin(\eta_m)}{\sinh(\zeta_m)\cos(\eta_p) + i\cosh(\zeta_m)\sin(\eta_p)}\right] \quad \text{(A.4)}$$

where

$$\zeta_m = \frac{\pi}{2K}(\zeta-\zeta_0), \quad \eta_m = \frac{\pi}{2K}(\eta-\eta_0) \quad \textit{and} \quad \eta_p = \frac{\pi}{2K}(\eta+\eta_0)$$

Similarly,

$$\bar{W}(\omega) = i\kappa \ln\left[\frac{\sinh(\zeta_m)\cos(\eta_m) - i\cosh(\zeta_m)\sin(\eta_m)}{\sinh(\zeta_m)\cos(\eta_p) - i\cosh(\zeta_m)\sin(\eta_p)}\right] \quad \text{(A.5)}$$

From $W(\omega) = \phi + i\psi$ *and* $\bar{W}(\omega) = \phi - i\psi$,

$$\psi = \frac{W(\omega) - \bar{W}(\omega)}{2i} \quad \text{(A.6)}$$

Substituting (A.4) and (A.5) in (A.6) gives:

$$\psi = \frac{-i\kappa \ln\left\{\left[\frac{\sinh(\zeta_m)\cos(\eta_m) + i\cosh(\zeta_m)\sin(\eta_m)}{\sinh(\zeta_m)\cos(\eta_p) + i\cosh(\zeta_m)\sin(\eta_m)}\right] - \left[\frac{\sinh(\zeta_m)\cos(\eta_m) - i\cosh(\zeta_m)\sin(\eta_m)}{\sinh(\zeta_m)\cos(\eta_p) - i\cosh(\zeta_m)\sin(\eta_m)}\right]\right\}}{2i}$$

$$= -\frac{\kappa}{2}\ln\left[\frac{\sinh^2(\zeta_m)\cos^2(\eta_m) + \cosh^2(\zeta_m)\sin^2(\eta_m)}{\sinh^2(\zeta_m)\cos^2(\eta_p) + \cosh^2(\zeta_m)\sin^2(\eta_p)}\right]$$

$$= -\frac{\kappa}{2}\ln\left[\frac{\sinh^2(\zeta_m) + \sin^2(\eta_m)}{\sinh^2(\zeta_m) + \sin^2(\eta_p)}\right]$$

$$= \frac{\kappa}{2}\ln\left[\frac{\sinh^2(\zeta_m) + \sin^2(\eta_p)}{\sinh^2(\zeta_m) + \sin^2(\eta_m)}\right]$$

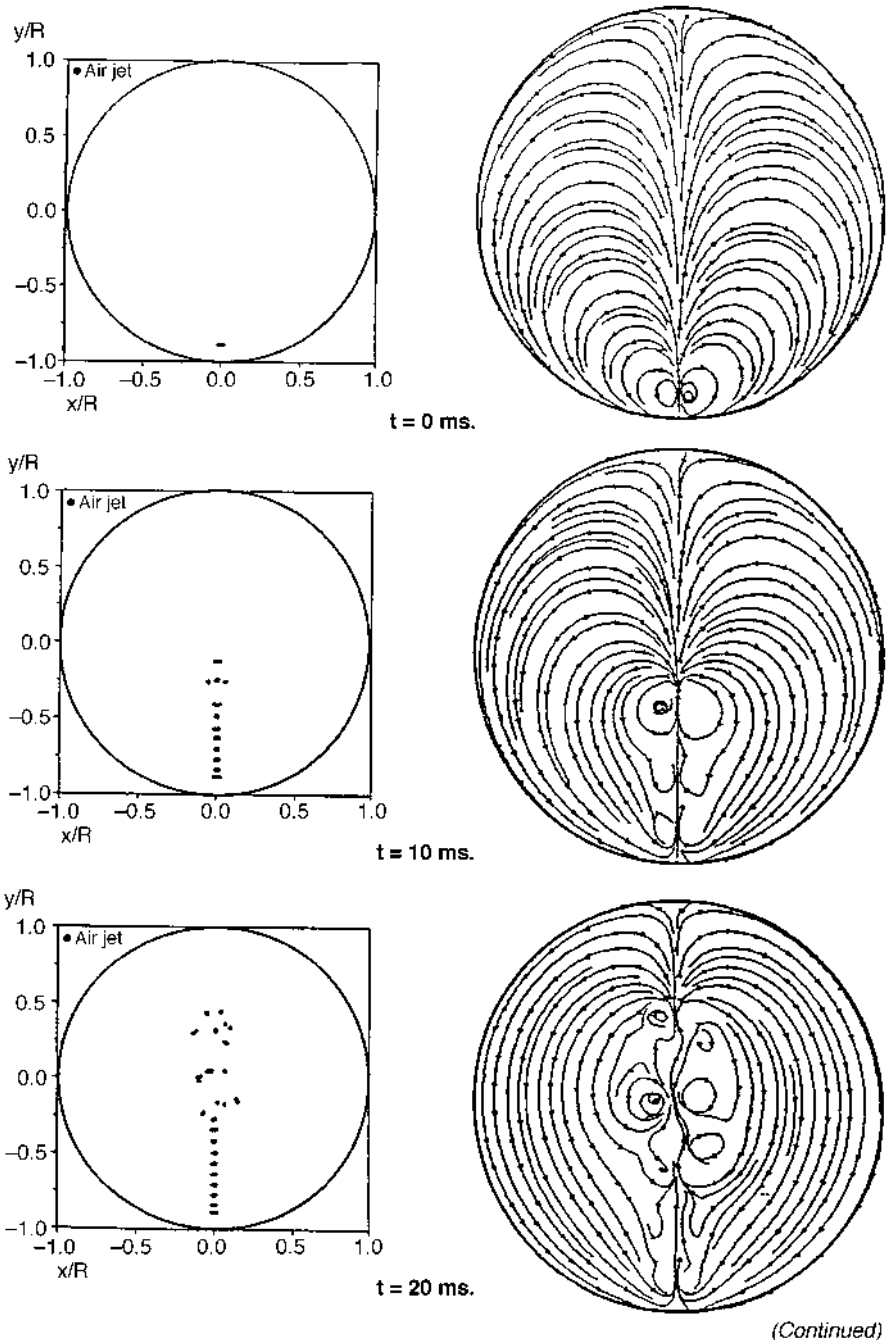

Figure A1.
Air jet particle trajectory and streamlines as a function of time (without swirl). Injector at 90 degrees (counterclockwise from horizontal).
U_{in} = 210.0m/s

(Continued)

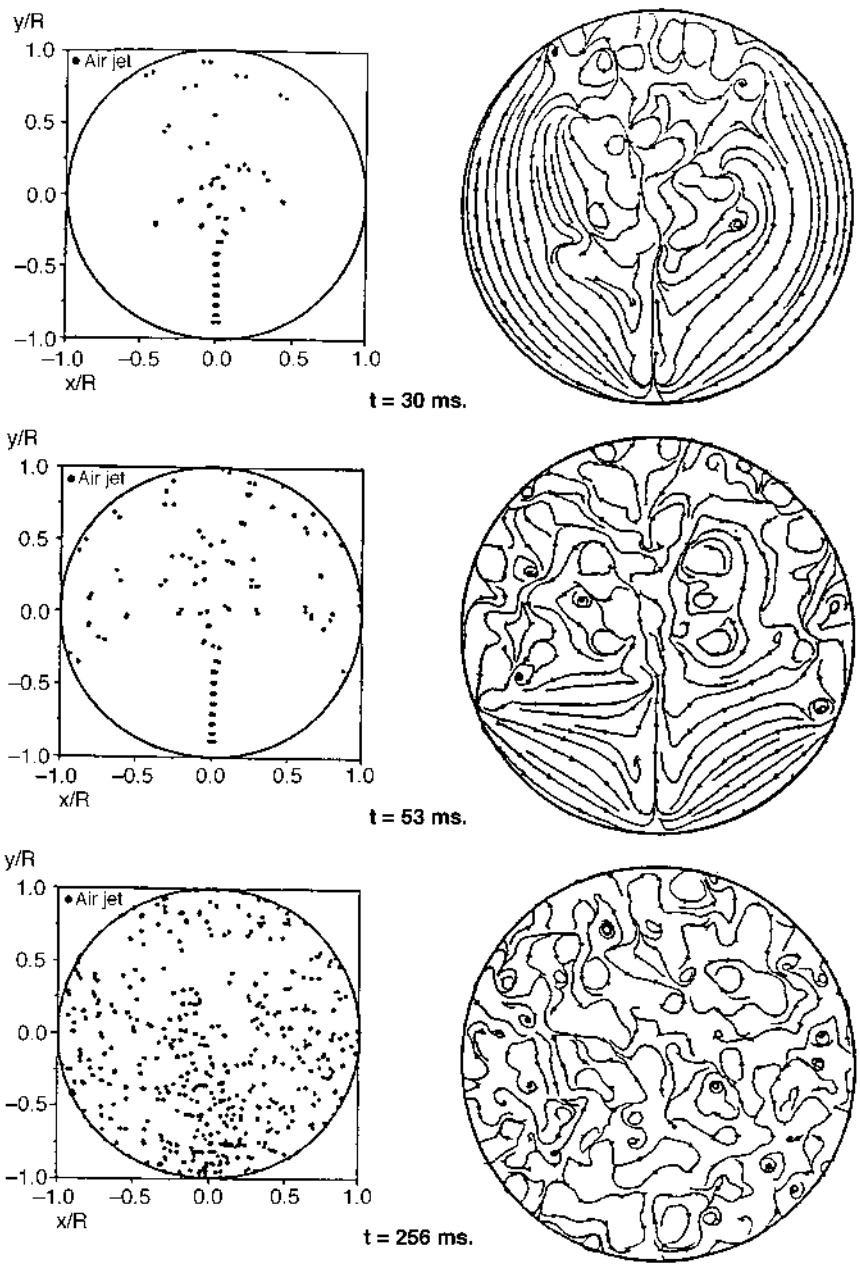

Figure A1.

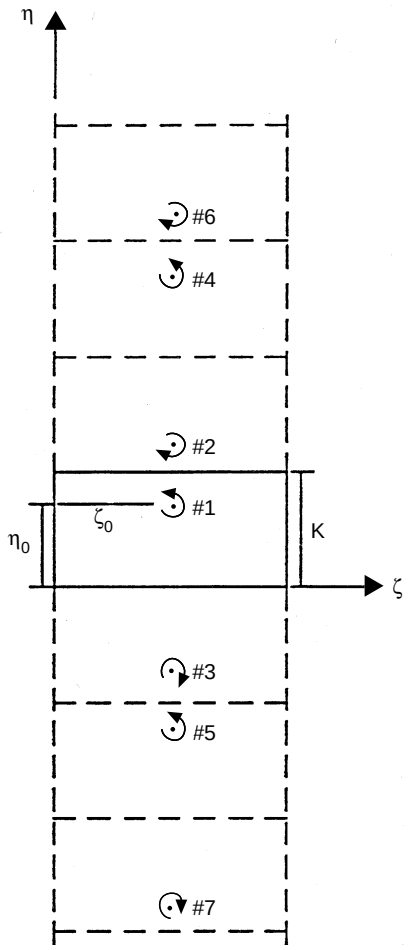

Figure A2.
Derivation of the streamfunction ψ inside a finite rectangular domain using method of images